JOURNAL OF AIRCRAFT
Vol. 51, No. 3, May–June 2014

Summary of the 2008 NASA Fundamental Aeronautics Program Sonic Boom Prediction Workshop

Michael A. Park*
NASA Langley Research Center, Hampton, Virginia 23681
Michael J. Aftosmis†
NASA Ames Research Center, Moffett Field, California 94035
Richard L. Campbell‡ and Melissa B. Carter§
NASA Langley Research Center, Hampton, Virginia 23681
Susan E. Cliff†
NASA Ames Research Center, Moffett Field, California 94035
and
Linda S. Bangert¶
NASA Langley Research Center, Hampton, Virginia 23681

DOI: 10.2514/1.C032589

The Supersonics Project of the NASA Fundamental Aeronautics Program organized an internal sonic boom workshop to evaluate near-field sonic-boom prediction capability at the Fundamental Aeronautics Annual Meeting in Atlanta, Georgia, on 8 October 2008. Workshop participants computed sonic-boom signatures for three nonlifting bodies and two lifting configurations. Cone–cylinder, parabolic, and quartic bodies of revolution comprised the nonlifting cases. The lifting configurations were a simple 69 deg delta-wing–body and a complete low-boom transport configuration designed during the High Speed Research Project in the 1990s with wing, body, tail, nacelle, and boundary-layer diverter components. The AIRPLANE, Cart3D, FUN3D, and USM3D flow solvers were employed with the ANET signature propagation tool, output-based adaptation, and a priori adaptation based on freestream Mach number and angle of attack. Results were presented orally at the workshop. This article documents the workshop and results and provides context on previously available and recently developed methods.

Nomenclature

dP	=	$(p - p_\infty)/p_\infty$, nondimensional pressure signature
h	=	distance below the model
J	=	adjoint cost function
L	=	line integral length
l	=	model length
Max E	=	maximum length of edge connected to node
p	=	pressure
r	=	radius
$ry1$, $ry2$	=	radius of elliptical/annular swept sector refinement region in y direction
$rz1$, $rz2$	=	radius of elliptical/annular swept sector refinement region in z direction
S	=	integration surface
u	=	x velocity
v	=	y velocity
w	=	z velocity
$x1$, $x2$	=	x extent of elliptical/annular swept sector refinement region

Subscript

∞	=	freestream value

Symbols

α	=	angle of attack
μ	=	Mach angle
ρ	=	density
φ	=	off-track angle

Presented as Paper 2013-0649 at the 51st Aerospace Sciences Meeting, Grapevine, TX, 7–10 January 2013; received 27 August 2013; accepted for publication 29 October 2013; published online 11 March 2014.

*Research Scientist, Computational AeroSciences Branch. Senior Member AIAA.
†Aerospace Engineer, Applied Modeling and Simulation Branch. Associate Fellow AIAA.
‡Senior Research Engineer, Configuration Aerodynamics Branch. Associate Fellow AIAA.
§Aerospace Engineer, Configuration Aerodynamics Branch. Senior Member AIAA.
¶Aerospace Engineer, Configuration Aerodynamics Branch. Associate Fellow AIAA.

I. Introduction

SUPERSONIC flights over land by civil aircraft are currently prohibited in many countries, including the United States. The acceptance of an aircraft's sonic boom to the general population and regulatory agencies is a requirement for supersonic flights over land and therefore the commercial viability of a supersonic transport. Predicting how sonic-boom signatures are perceived is a challenging task that requires the prediction of the signature on the ground. This is a task complicated by long propagation distances, atmospheric variations, and the Earth's turbulent boundary layer [1]. A detailed review of the history and state-of-the-art of sonic-boom modeling is provided by Plotkin [2]. Surveys of sonic-boom prediction methods are available from Ozcer [3] and Park [4].

The propagation of a sonic boom is often separated into two logical stages or regions, depicted in Fig. 1, to facilitate analysis. The near field is a region near the aircraft, where shocks are formed and strongly influenced by nonlinear phenomena such as shock–shock interaction, shock curvature, and cross flow. Computational fluid dynamics (CFD) methods are typically employed in this near-field region, denoted CFD domain in Fig. 1, to capture these phenomena. Higher-pressure portions of the signature travel faster than lower-

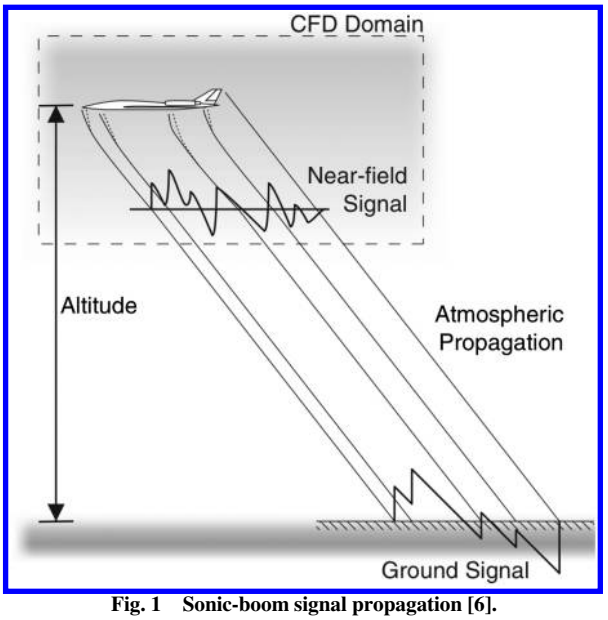

Fig. 1 Sonic-boom signal propagation [6].

pressure portions of the signature because of variations in the local speed of sound. This slight speed difference causes the expansions to elongate and the shocks to coalesce as they propagate. Sonic-boom propagation methods [5] are typically employed in the far field, where the geometric details of the configuration are less important than atmospheric variations and molecular relaxation phenomena. These atmospheric propagation methods rely on the availability of an accurate near-field signature.

The NASA Fundamental Aeronautics Program Supersonics Project held a workshop at the 2008 Fundamental Aeronautics Annual Meeting in Atlanta, Georgia, to evaluate NASA's capability to predict the near-field signatures of simple and complex geometries. The participants provided method descriptions at the workshop, and a summary presentation was prepared. Table 1 is the workshop agenda listing the duration, titles, and authors of the oral presentations. Table 2 is a listing of the models considered in the workshop. This article summarizes the results presented at the 2008 workshop as well as places the workshop in the context of previous work and developments that took place after the workshop.

II. Near-Field Sonic-Boom Prediction Methods Available at NASA Before the Workshop

Early work applied CFD within a fraction of a body length. This very near-body signature was propagated to the wind-tunnel measurement locations with ANET [11]. Cheung et al. [12] applied UPS3D with ANET to cone–cylinder, wing, and delta-wing–body configurations. Cliff and Thomas [13] applied FLO60, TEAM, and AIRPLANE with ANET to the same cone–cylinder, wing, and delta-wing–body configurations. Madson [14] applied TranAir to these same configurations. Cliff et al. [10,15] applied HFLO4 and AIRPLANE with ANET to a wing–body nacelle tail at near-field distances from 1/4 to 1/3 of a body length. Djomehri and Erickson [16] applied an adaptive unstructured grid FELISA method with ANET to airfoil, cone–cylinder, wing, and delta-wing–body configurations.

Fouladi [17] applied linear VGRID sources and USM3D to isotropic grids of a body of revolution. Carter and Deere [18] examined a number of grid sourcing methods in VGRID and the grid adaptation methods ADAPT, ADV, and CRISP. The SSGRID grid modification tool, an a priori adaptation method used in the workshop, was also introduced. Campbell et al. [19] provides a more detailed description of ADV and SSGRID. Pirzadeh [20] developed a volume sourcing method that allows for specification of a swept and refined volume region below an aircraft configuration.

Before the workshop, FUN3D had an existing anisotropic output adaptation scheme for tetrahedral body-fitted grids [21]. Lee-Rausch et al. [22] examined the near-body signatures of cone–cylinder and wing–body configurations, and Jones et al. [23] performed detailed validation exercises on cone–cylinder geometries. The body-fitted approach to adaptive gridding exhibited robustness difficulties near curved surfaces that were alleviated by the cut-cell approach used at the workshop.

In early 2008, Nemec et al. [24] used Cart3D along with adjoint-based mesh adaptation to predict the pressure signature of a diamond airfoil. This work used both an off-body functional to drive the adjoint and introduced a mesh alignment technique based on the Mach angle of the freestream flow. The capability was built upon a preexisting mesh adaptation scheme [25] and adjoint solver [26]. Three-dimensional (3-D) examples using the Cartesian adjoint approach were presented in June 2008, including many cases similar to those used in the workshop [27].

III. Methods

There are five methods used in this study. Accurately predicting near-field signatures is a challenging task that requires the combination of a flow solver with a specialty grid generation or grid adaptation technique. A signature propagation technique is also employed in conjunction with the flow solver for two methods. A detailed description of each method is provided in the following sections.

Table 1 2008 NASA Fundamental Aeronautics Program Sonic Boom Prediction Workshop agenda

Duration	Lecture
15 min.	"Introduction and Case Descriptions for the Sonic Boom Prediction Workshop," Susan Cliff, NASA Ames
45 min.	"Assessment of Unstructured Euler Methods for Sonic Boom Pressure Signatures Using Grid Refinement and Domain Rotation Methods," Susan Cliff, Scott Thomas, Matt McMullen, John Melton, and Don Durston, NASA Ames Research Center
30 min.	"Output-Adaptive Tetrahedral Cut-Cell Validation for Sonic Boom Prediction," Michael Park and Eric Nielsen, NASA Langley Research Center
30 min.	"Sonic-Boom Prediction with Output-Based Adaptation and Cart3D," Michael Aftosmis, Marian Nemec, and Mathias Wintzer, NASA Ames Research Center
30 min.	"A Method for Shearing and Stretching Unstructured Grids for Improved Sonic Boom Prediction, Richard Campbell and Melissa Carter," NASA Langley Research Center
30 min.	"Summary and Comparison of NASA's Supersonic Boom Prediction Methods," Melissa Carter, NASA Langley Research Center

Table 2 Sonic Boom Prediction Workshop models

Configuration	Mach number	Angle of attack	h/l	Report
6.48 deg cone–cylinder	1.68	0.0	10.0	NASA TM X-2219 [7]
Parabolic body of revolution	1.41	0.0	10.0	NASA TN D-3106 [8]
Quartic body of revolution	1.41	0.0	10.0	NASA TN D-3106 [8]
69 deg swept delta-wing body	1.68	4.74	3.6	NASA TN D-7160 [9]
Ames low boom wing tail with four nacelles	2.0	2.0	1.167	NASA CP-1999-209699 [10]

A. Component Techniques

The ANET, EASS, and Cart3D techniques are each used by two of the methods, and so they will be described first in subsections. AIRPLANE–ANET and Cart3D–ANET use AIRPLANE and Cart3D flow solvers to propagate the signatures less than one body length and transfer the solution to ANET, a signature propagation tool. Cart3D–adjoint combines the Cart3D flow solver with an adjoint-based adaptation scheme. FUN3D–adjoint uses a similar adjoint-based adaptation scheme, but uses a tetrahedral background grid. USM3D–SSGRID is the USM3D flow solver used directly with a priori grid shearing and stretching of a baseline isotropic grid.

1. *ANET*

ANET is a sonic-boom propagation code originally developed by Thomas [11]. It uses a waveform parameter method [28] where the signature is completely described by a set of parameters. Equations are obtained for the time rates of change of these parameters and integrated in time to propagate the signature. ANET is typically used with a standard atmospheric model to propagate the near-field signature to the ground. When combined with AIRPLANE and Cart3D in this article, a uniform atmospheric model is assumed to propagate the signature within the wind-tunnel test section.

2. *Elliptical/Annular Swept Sector*

Mesh generation techniques for external flows typically have a fine grid near the model that coarsens away from the model until the outer boundary is reached. Accurate off-body signature prediction requires constant spacing in important propagation regions. This region of constant spacing is described as the elliptical/annular swept sector (EASS), depicted in Fig. 2.

The regions in Fig. 2 are described by providing the Mach number, $x1$, $x2$, $ry1$, $ry2$, $rz1$, $rz2$, and off-track angle φ. The region can be annular when $ry1$ and $rz1$ are greater than zero. Most often, they are defined to be circular in the front view by setting $ry1 = rz1$ and $ry2 = rz2$. Elliptically shaped refinement regions can be used when the region of the aircraft is noncircular, such as a winged configuration in axial cross section. Refinement regions or "sectors" are rotated for azimuthal angles from 0 (below the aircraft) to a user-prescribed angle φ up to 180 deg.

3. *Cart3D*

The Cart3D package uses a Cartesian cut-cell approach [29] in which the governing equations are discretized on a multilevel Cartesian mesh with embedded boundaries. The Cart3D flow solver is combined with the ANET propagation method and an adjoint-based grid adaptation scheme, which are described in the following sections. The mesh consists of regular Cartesian hexahedra everywhere, except for a layer of body-intersecting boundaries as illustrated in Fig. 3. A finite-volume method is applied in the computational domain with a weak imposition of boundary conditions.

Although it consists of nested Cartesian cells, the mesh is viewed as an unstructured collection of control volumes, making the approach well-suited for solution-adaptive mesh refinement. The refinement is performed in discrete refinement levels, where a cell is split in the Cartesian directions. Figure 3 illustrates two refinement levels: the large squares on the left and the small squares on the right. Steady-state flow solutions are obtained using a five-stage Runge–Kutta scheme with local time stepping and multigrid. The flux-vector splitting approach of van Leer [30] is used. Domain decomposition via space-filling curves permits parallel computation; for more details, see Aftosmis et al. [31,32] and Berger et al. [33].

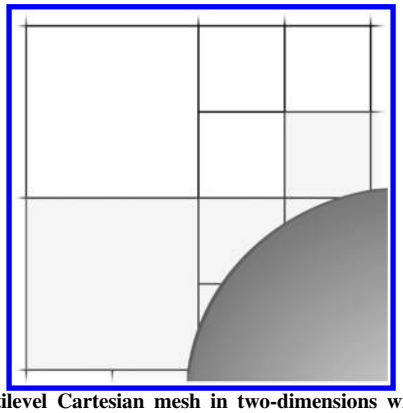

Fig. 3 Multilevel Cartesian mesh in two-dimensions with a cut-cell boundary.

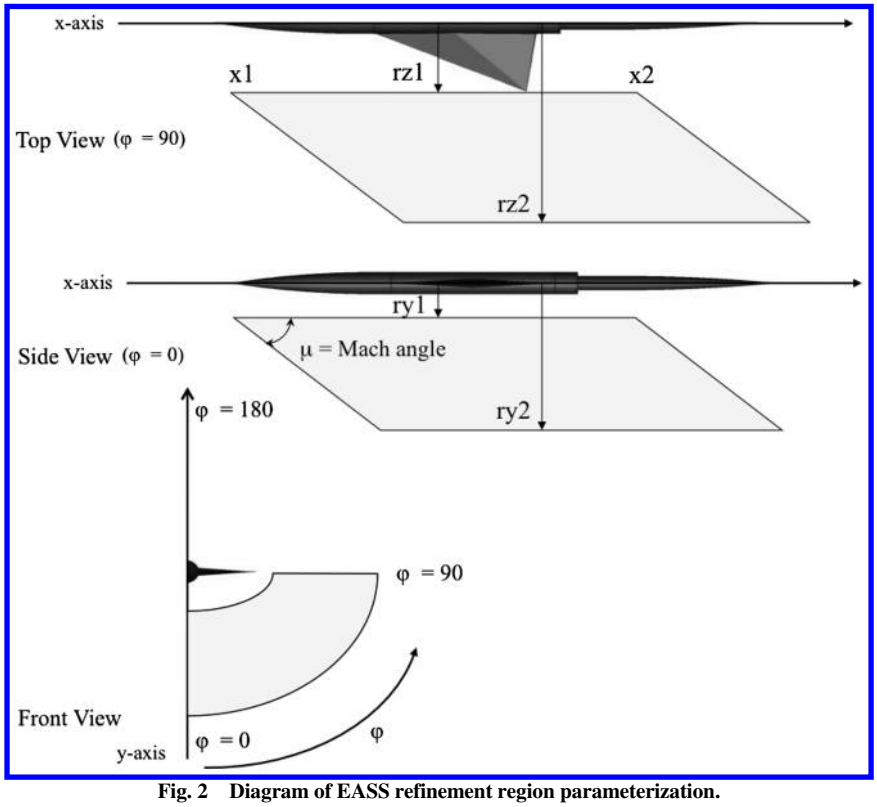

Fig. 2 Diagram of EASS refinement region parameterization.

In boom propagation problems, the Cartesian mesh is rotated to roughly align the mesh cells with the freestream Mach wave angle. Mesh rotation also permits the cells stretching along the dominant wave propagation direction to directly increase the per-cell signal propagation distance. Details of these techniques are available in Wintzer et al. [27]. Nemec et al. [24] demonstrate a saving of 3 in grid size with equivalent accuracy in a two-dimensional (2-D) example due to rotation and anisotropic refinement with aspect ratio of 4. Saving a factor of 16 in 3-D grid size with equivalent accuracy by rotation is documented by Cliff et al. [34].

B. AIRPLANE–ANET

The AIRPLANE–ANET method [34] is an Euler unstructured-tetrahedra-grid method [35,36]. The mesh generator in its original formulation provided a smooth gradation from the fine surface mesh to the coarse far-field boundaries. This smooth gradation of the volume mesh density is not ideal for sonic-boom computations because the off-body mesh coarsens too quickly. To increase the mesh density within the sonic-boom region of influence so that the pressure signature can be propagated sufficiently far from the model, the mesh generator was modified to allow a user to refine meshes in specified regions for sonic-boom computations. This refinement region is defined with EASS.

Automatic cell refinement based on the edge length and distance from the model is employed. Figure 4 shows three axial slices of the 69 deg delta-wing–body and sting configuration colored by the maximum edge length, "Max E". Conditional splitting based on edge length allows for smoother changes in grid densities and simplifies the process by only requiring one EASS region.

EASS refinement permits a fairly efficient use of mesh points with increased accuracy for boom assessment, provided the aircraft bow and tail shocks stay within the EASS. Pressure signatures were extracted in the very near field at 0.4 body lengths below the configuration and propagated to wind-tunnel test altitudes with ANET via a uniform atmosphere model.

C. Cart3D–ANET

In the Cart3D–ANET approach [34], the basic Cartesian method is used either with or without mesh rotation and is combined with EASS mesh refinement specification. The independence of the surface grid is advantageous in sonic-boom analysis because the effects of volume grid density can be studied independently of the surface grid density, and the effects of grid variations can be easily assessed.

EASS refinement regions were implemented in Cart3D by the development of a software tool that generates the defining input of a large number of rectangular regions that fill an EASS refinement region. These rectangular regions are provided to Cart3D to trigger refinement [25], as seen in Fig. 5. The swept refinement region can be accurately prescribed with the large number of small rectangular regions inside the expected zone of influence of the solutions, and a single level of Cartesian mesh refinement throughout the EASS region can be easily obtained. This allows for simple grid-refinement

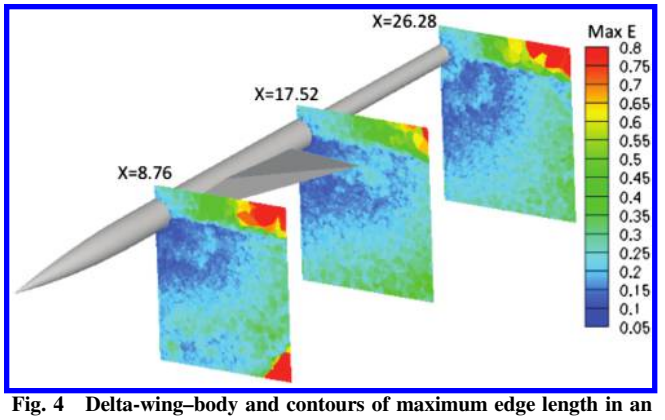

Fig. 4 Delta-wing–body and contours of maximum edge length in an EASS region.

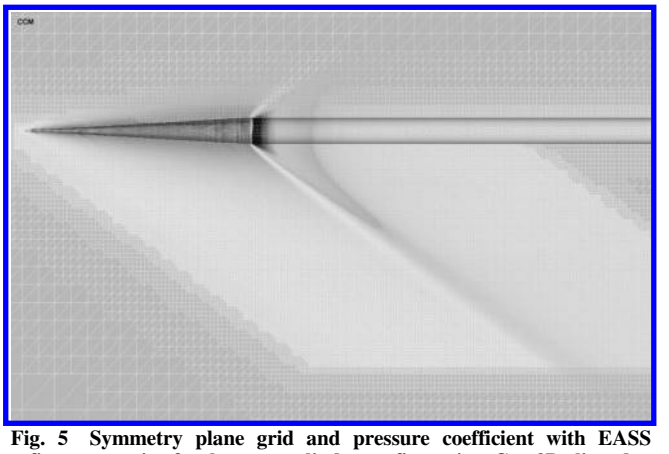

Fig. 5 Symmetry plane grid and pressure coefficient with EASS refinement region for the cone–cylinder configuration, Cart3D aligned to the x axis, Mach 1.68, $\alpha = 0.0$ deg.

studies with Cart3D to compare the differential pressure distribution with mesh refinement level [34]. The level of refinement shown in Fig. 5 is what was required to obtain accurate pressure signatures near the boundaries of the EASS region [34].

EASS refinement was also combined with mesh rotation to the dominant propagation direction. This resulted in significant savings in the required computational mesh size for the same level of accuracy as nonrotated cases. Saving a factor of 16 in grid size with equivalent accuracy by rotation is documented by Cliff et al. [34]. Figure 6 shows the same configuration at equivalent accuracy as Fig. 5 with a factor of 16 smaller grid.

D. Cart3D–Adjoint

In 2005, a duality-preserving discrete adjoint approach was introduced for Cart3D by Nemec and Aftosmis [26] for aerodynamic shape optimization. This adjoint solver shares the same basic data structures, domain decomposition, and other infrastructure with the primal solver and achieves similar performance. Nemec and Aftosmis [37] first applied this method for output error estimation and adaptive refinement in 2007 using an approach similar to that of Venditti and Darmofal [38] and others [39–41]. In 2008, it was applied for boom-propagation problems using a quadratic form of the pressure p:

$$\mathcal{J} = \int_0^L \left(\frac{p - p_\infty}{p_\infty} \right)^2 \mathrm{d}l \tag{1}$$

where the integration is performed along a sensor of length L placed in the field where the signature is measured.

The adjoint-based error estimation then tailors the mesh refinement to reduce the error in the pressure signature at the

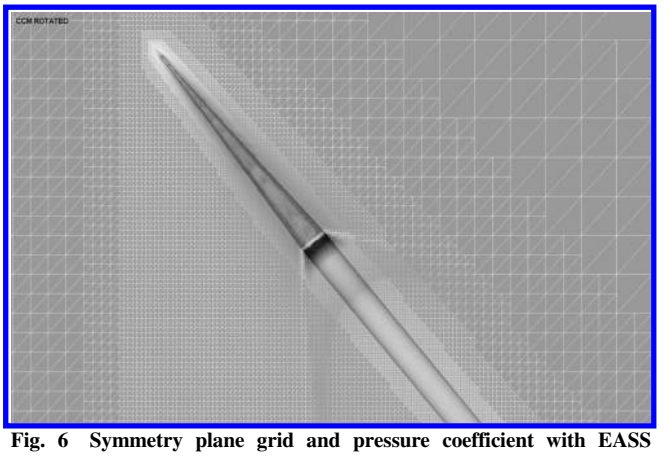

Fig. 6 Symmetry plane grid and pressure coefficient with EASS refinement region for the cone–cylinder configuration, Cart3D aligned to freestream Mach angle, Mach 1.68, $\alpha = 0.0$ deg.

location of the sensor. Error in this signal can be either driven below some specified value or, alternatively, reduced as much as possible using a worst-errors-first strategy for a desired mesh size. Adaptation is performed incrementally by cycling between the primal and adjoint solvers, with no more than one level of cell refinement being performed at a time. With this strategy, typical simulations cost 3–5 times that of a single flow solve on the final mesh. Figure 7 shows a typical mesh produced by this method for flow over an axisymmetric body at Mach 1.6 and 0 deg angle of attack. The mesh was produced after 11 cycles of adaptive refinement driven by the pressure signature from the shaded portion of the body on an array of four sensors located 1.8 body lengths $h/l = 1.8$ away. This verification example from Aftosmis et al. [6] shows that the pressures along all sensors collapse to the same signature, as expected in axisymmetric flow.

E. FUN3D–Adjoint

The FUN3D–adjoint method is an output-adaptive cut-cell method using tetrahedral background grids. The complete adaptive process is documented by Park [4]. The cut-cell flow solver including gradient reconstruction and limiting is summarized by Park and Darmofal [42], and the parallel grid mechanics are summarized by Park and Darmofal [43].

A triangulated surface mesh of the geometry is Boolean subtracted from the median duals of the background grid to form the computational domain. To introduce the 3-D cut-cell method, a simple 2-D example is presented. The primal triangular grid is shown in Fig. 8a. The control volumes used by the flow solver are the median duals of this triangular mesh in Fig. 8b. These median duals are constructed by gathering the three dual faces that are inside each primal triangle. These faces connect the center of the triangle to the midpoints of its edges. The geometry in this example is a diamond airfoil, shown with the uncut median dual background grid in Fig. 8c. The airfoil geometry is Boolean subtracted from this background grid, removing the portion of the background grid that is external to the flow domain (Fig. 8d). This is the same operation that Cart3D performs, but here the background grid is tetrahedral instead of Cartesian. The result of the Boolean subtraction are the control volumes used by the flow and adjoint solver.

Weighted least-squares reconstruction is performed to increase the accuracy of the scheme. These reconstructed gradients are reduced with a continuously differentiable heuristic limiter that permits good iterative convergence [42]. Backward facing steps (e.g., blunt trailing edges) can create strong expansions in Euler flows. These strong expansions can create difficulties for approximate Riemann solvers. A transpiration boundary condition is applied to boundary faces with downstream-pointing normals to lessen the strength of these expansions while retaining some of the characteristics of wake flows. This boundary condition applies freestream velocity state u_∞, v_∞, and w_∞ with a density and pressure of $\rho = 0.3\rho_\infty$ and $p = 0.3p_\infty$ [4].

An exact discrete adjoint solution is computed based on a pressure p based sonic-boom sensor cost function:

$$\mathcal{J} = \iint_S \left(\frac{p - p_\infty}{p_\infty}\right)^2 \mathrm{d}s \tag{2}$$

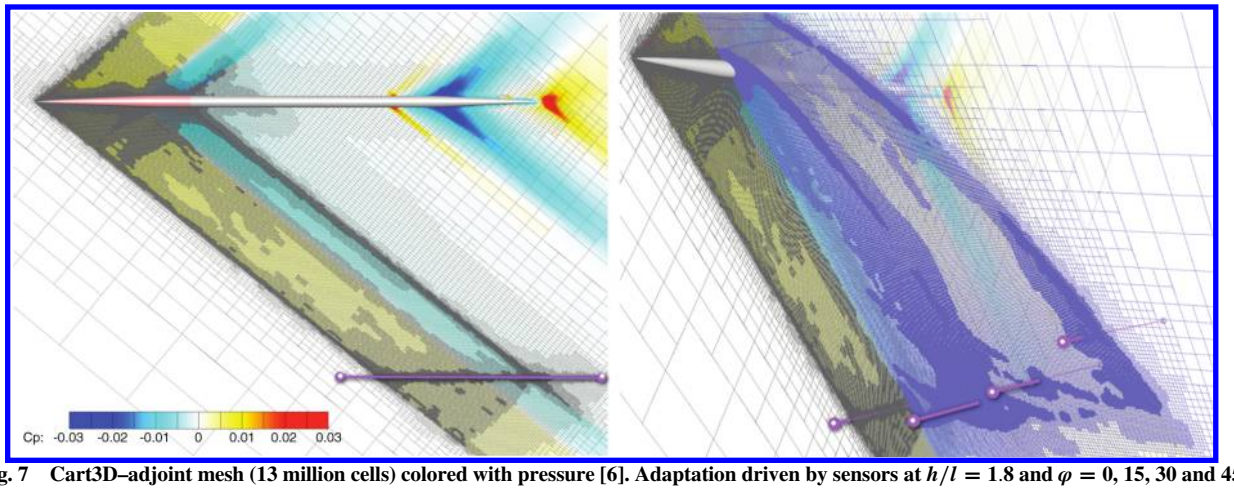

Fig. 7 Cart3D–adjoint mesh (13 million cells) colored with pressure [6]. Adaptation driven by sensors at $h/l = 1.8$ and $\varphi = 0$, 15, 30 and 45.

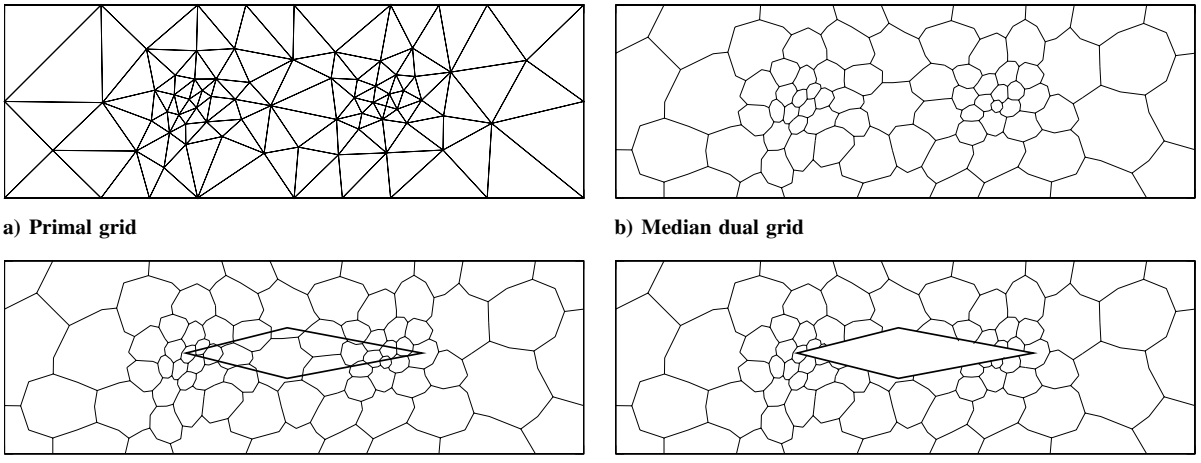

a) Primal grid **b) Median dual grid**

c) Median dual grid with geometry **d) Resulting cut-cell grid**

Fig. 8 Cut-cell illustration of a diamond airfoil in 2-D with a simplex background grid.

integrated over a cylindrical surface S centered at the model that passes through the wind-tunnel measurement locations. The primal and adjoint solution are reconstructed on the grid with two methods. These different reconstructions are employed to form an adaptive indicator [4]. This adaptive indicator is combined with the Mach Hessian to compute the requested metric for the background grid; see Venditti and Darmofal [44]. A parallel grid adaptation scheme [4,43] is applied to the background grid to produce a new background grid based on the requested metric. This adaptive process is applied multiple times until the resolved pressure signature at the sensor location is available. The initial and final symmetry plane grid of an axisymmetric configuration [45] are shown in Fig. 9 to illustrate this process. The extremely coarse isotropic initial grid (Fig. 9a) is created independently of Mach number or angle of attack. There is no attempt to represent the propagation of the shocks to the sensor location, only the geometry in the upper right is partially resolved. After 17 adaptation cycles, the final grid (Fig. 9b) accurately resolves the signature at $h/l = 6$.

The use of cut cells with an output-based adaptive scheme automates the volume grid generation task after the triangular surface mesh is generated. This robust adaptation scheme allows extremely coarse isotropic initial grids that can be generated without a priori knowledge of shock locations or Mach angles. The general anisotropy of the adapted background grids allows for accurate center line and off-center line signal prediction [42].

F. USM3D–SSGRID

The TetrUSS CFD software package [46] includes the VGRID grid generation code [47] along with the USM3D Navier–Stokes flow solver [48]. The VGRID code uses a combination of the advancing layer and advancing front methods to fill the computational domain with tetrahedral cells. The grid spacing on the configuration surfaces, outer boundaries, domain interior is related to the strength of sources placed in the domain. Although point and line sources can be used to control field grid density, the resulting grid density can be nonuniform. A more recently developed source type, the volume source [20], allows much better control of field grid spacing and is discussed further in the following section.

The USM3D code is a cell-centered, finite-volume Navier–Stokes flow solver that uses Roe flux-difference splitting [49] to compute inviscid flux quantities across the faces of the tetrahedral cells. The parallel version of the flow solver was run inviscidly using the implicit mode for the cases presented in this study. The minmod limiter was typically used to ensure numerical stability during the initial iterations and was then turned off for the final cycles to minimize dissipation in the sonic-boom signature.

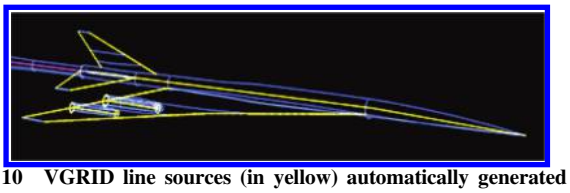

Fig. 10 VGRID line sources (in yellow) automatically generated by AUTOSRC.

1. *Automated Source Placement for Grid Generation*

The geometry is defined with GRIDTOOL [50]. VGRID requires a specification of the requested grid density in the form of sources [20,51] to convert this geometry definition into a grid. AUTOSRC is developed to provide an automated, knowledge-based approach to the placement and sizing of these VGRID sources. AUTOSRC identifies key geometry curves for the patches associated with components such as the fuselage, wing, winglet, nacelles, pylons, canard, and horizontal and vertical tails, then uses this information to determine line source location and grid spacing size.

Figure 10 illustrates how the sources (yellow lines) are placed along the leading and trailing edges of lifting surfaces and down the centerline of the fuselage. The source layout for nacelles includes a ring of line sources around the inlet and exit as well as a streamwise source down the centerline of the nacelle.

In addition to the automated layout of line sources described previously, two options that use the new volume source capability in VGRID [20] have been included in AUTOSRC. The first option is used for the computation of the near-field sonic-boom signature of an aircraft and involves placing a vertical-axis cylindrical volume source just below the fuselage. This volume source is automatically sized and located under the configuration to provide a dense field grid for resolving shocks and expansions (see the yellow cylinder around the dashed center line in Fig. 11). This grid is further modified by the SSGRID code, which is described in the next subsection, to help reduce dissipation in the flow solution. The second option places a horizontal-axis cylindrical source behind the nacelle exit to create a denser grid to resolve the engine plume shape for powered simulations (see the magenta cylinder in Fig. 11). Currently, the length of the plume source is a user input, with a recommended value of three nacelle lengths based on limited experience. Further details on the AUTOSRC method can be found in Li et al. [52].

2. *Stretching and Shearing of the Field Grid*

As mentioned in the previous section, the initial grid is typically generated with VGRID using fairly large grid spacing away from the body, except for a region of dense grid underneath the vehicle that is

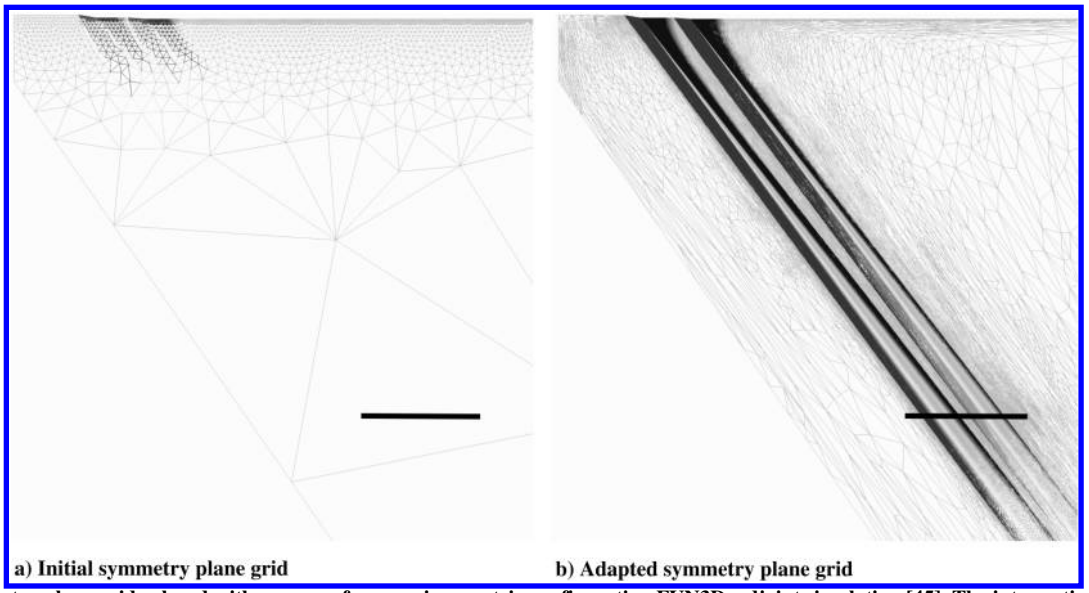

Fig. 9 Symmetry plane grid colored with pressure for an axisymmetric configuration FUN3D–adjoint simulation [45]. The intersection of the sensor surface with the symmetry plane is shown in black.

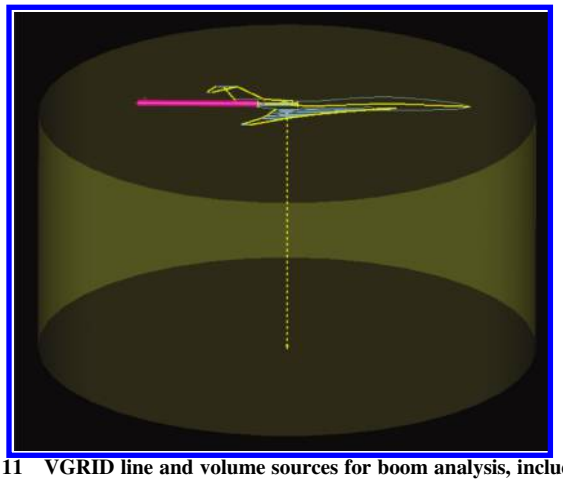

Fig. 11 VGRID line and volume sources for boom analysis, including plume effects.

created using a cylindrical volume source. The left side of Fig. 12 shows the grid generated for the symmetry plane using this technique. Although this approach does improve the propagation of flow features in the dense zone relative to outer coarse grid regions, it significantly increases the number of grid cells and is thus not practical for use in reaching the typical near-field location of 3–5 body lengths below the aircraft. In general, the cell faces are not aligned with the flow features, which are dissipated as they pass through the skewed faces.

The SSGRID code was developed to address these issues by shearing and stretching the original grid along Mach lines. This process allows fewer grid points to be used to reach a given signature location and aligns the cell faces with the flow features to reduce dissipation. Because shearing the grid close to the body might cause it to intersect the wings or other components, an inner cylinder parallel to the body axis and just outside the wing tip is defined, within which no grid modification occurs; see Fig. 13. This region tends to be much farther from the keel line of the aircraft than it needs to be and could allow unnecessary dissipation to occur before the sheared grid is reached. To remedy this, a variable inner cylinder radius is used based on the keel line. The keel line, primary inner cylinder radius, and variable radius are all automatically determined in SSGRID based on the aircraft geometry and initial grid characteristics. The right side of Fig. 12 illustrates the extent of a typical stretched and skewed grid, with the small blue region corresponding to the grid portion shown in the lower half of Fig. 13. The previous figures are from Li et al. [52], where a more detailed description of SSGRID can be found.

IV. Test Cases and Results

The methods were examined by analysis of five configurations ranging from simple axisymmetric models to lifting models with fuselage, wing, tail, and nacelles; see Table 2. All of the analyses for the workshop assumed inviscid flow. The primary focus of the

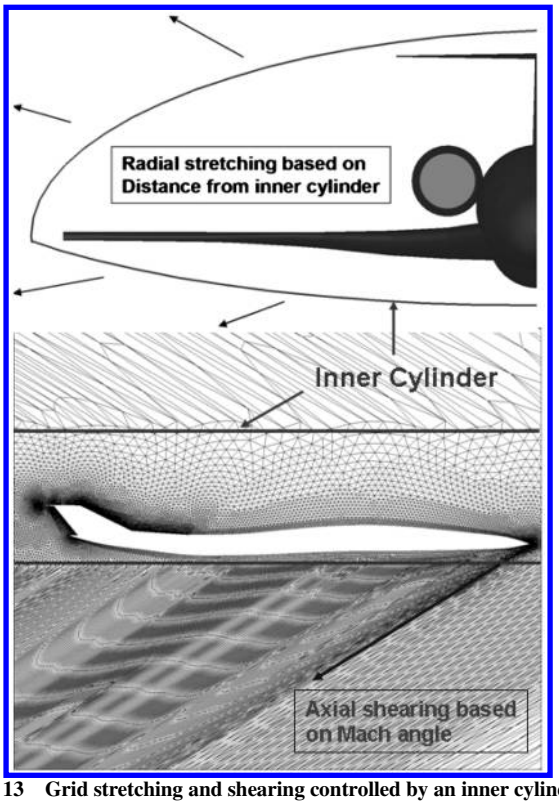

Fig. 13 Grid stretching and shearing controlled by an inner cylinder.

workshop was code-to-code comparisons. Wind-tunnel measurements are provided for reference, but there are known differences between the wind-tunnel test and CFD simulation that are expected to prevent a perfect match of measured and predicted results.

The analyses assumed steady uniform flow. However, wind tunnels have varying degrees of flow nonuniformity (spatial and temporal fluctuations in Mach number, static pressure, and humidity) [53–55], and the models are subject to aeroelastic effects because they are slender and have thin wing sections. These dynamic deformations can cause a 10–20% variation in normal force, which is used to infer angle of attack. The flow nonuniformity also smears shocks, increasing their measured thickness [56]. The reference pressure probe is in a different location in the tunnel than the measurement probe, which is an additional source of uncertainty. Because measurements were taken at discrete locations in the tunnel, the maximum of the shock peak or minimum of the expansion pressure may have been missed.

The viscosity effects in the measured data are not captured by the Euler computations. An effect of the boundary layer and boundary-layer tripping on the measured near-field signatures has been observed by Wayman et al. [57]. The wind-tunnel model base and sting geometry are not documented in the references for the lifting cases, and so the different methods used for modeling this juncture

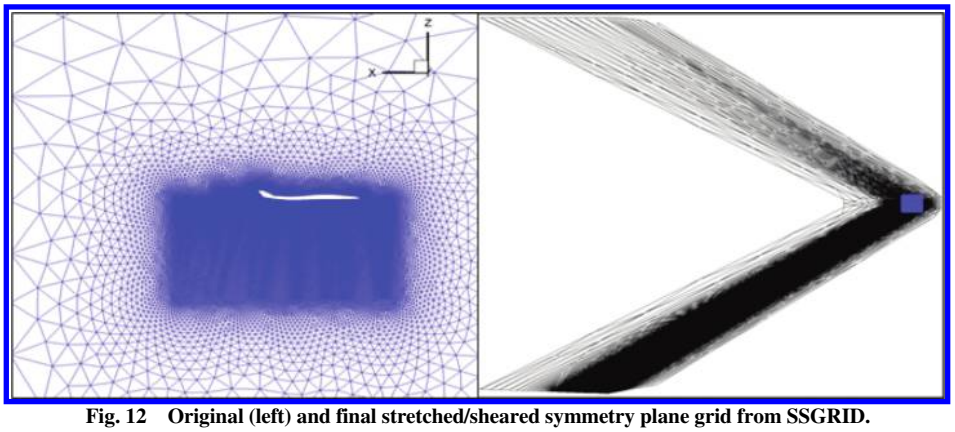

Fig. 12 Original (left) and final stretched/sheared symmetry plane grid from SSGRID.

are discussed in the relevant subsequent sections. Also, manufactured model geometry may differ slightly from the definitions used in analysis.

Because of slight variations in wind-tunnel Mach number, the computed signatures in the following section are shifted slightly in x/l to facilitate comparison. A single obvious feature is selected for each signature, and the computed signatures are shifted in x/l until the location of this feature is aligned with the wind-tunnel measurements. A uniform expansion is an ideal feature, but a shock location was selected for the lifting cases, which lack a uniform expansion.

A. Cone–Cylinder

The 6.48 deg Cone–cylinder is denoted as Model I(a) in Mendoza and Hicks [7]. The Mach number is 1.68, and the angle of attack is zero. The signature was measured at an altitude of 86 in., which is at 10 body lengths. The body is defined as the cone in Fig. 14, which has a 8.6 in. reference length. This configuration was chosen because it represents a near-field pressure signature with finite rise time.

The signatures from all methods are compared with experimental measurements digitized from the report [7], which are the filled circles in Fig. 15. The vertical axis dP is the normalized disturbance pressure $(p - p_\infty)/p_\infty$. The horizontal axis is x normalized by the model length l. The signatures have been shifted slightly in x/l to match pressure at the center of the expansion at $x/l = 1.1$ because the location of this expansion is an obvious feature of all the available signatures. The methods involving ANET propagation have lower slopes for the initial compression and shoulder expansion where the cone intersects the cylinder. This lower slope results in the most forward maximum pressure location and most aft minimum pressure location. Other methods are very difficult to distinguish, except for the details of undershoot at $x/l = 1.3$. FUN3D–adjoint has the lowest pressure at the end of the expansion and agrees with Cart3D–adjoint and USM3D–SSGRID on the location of lowest pressure. The workshop participants noted that details of the signal maximums and minimums at the workshop could be adjusted with reconstruction limiters. Campbell et al. [19] show an increase in the minimum pressure with the use of a limiter for this cone–cylinder configuration. Park and Darmofal [42] also show that the signature extrema can be adjusted with the choice of limiter.

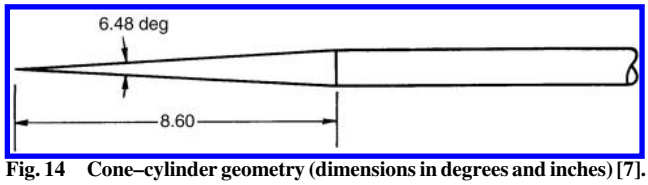

Fig. 14 Cone–cylinder geometry (dimensions in degrees and inches) [7]. The model is defined as the cone.

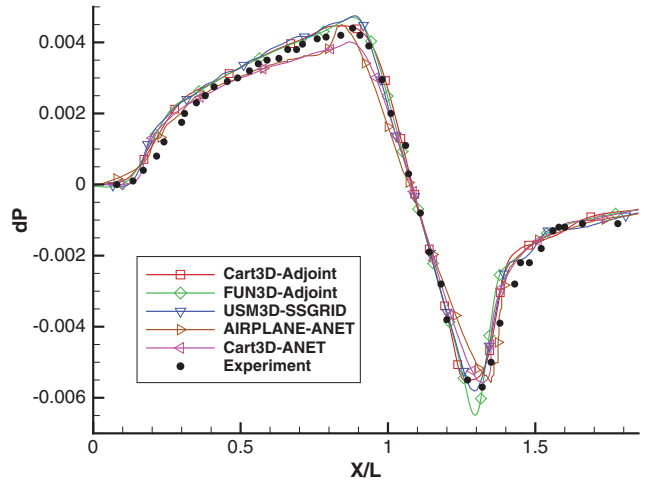

Fig. 15 Nondimensional pressure signature for the cone–cylinder geometry at $h/l = 10.0$.

This cone–cylinder configuration is considered a good configuration for benchmarking simulation. Cone–cylinder results were published before the workshop by a number of researchers, providing a good history of how this field of prediction has progressed. Cheung et al. [12] applied UPS3D. Cliff and Thomas [13] applied TEAM and AIRPLANE to 1.1 and 0.1 body lengths and propagated these near-field signatures with ANET to the wind-tunnel measurements at 10 body lengths. Madson [14] applied TranAir to 0.25 body lengths and propagated these near-field signatures with ANET to the wind-tunnel measurements at 10 and 20 body lengths. Djomehri and Erickson [16] applied an adaptive grid FELISA method to 0.4 body lengths, which was propagated with ANET to 10 body lengths.

B. Parabolic

The parabolic body of revolution is denoted as Model 4 in Carlson et al. [8]. The radius r of the model as a function of x is

$$r(x) = \sqrt{\frac{0.02}{\pi}x} \tag{3}$$

See Fig. 16. The Mach number is 1.41, and the angle of attack is zero. The signature was measured at an altitude of 20 in., which is 10 body lengths of the 2.0 in. model. This configuration was chosen because it is representative of the nose of a typical supersonic transport design.

The signatures from all methods are compared with experimental measurements digitized from the report [8], which are the filled circles in Fig. 17. The signatures have been shifted slightly in x/l to match pressure at the center of the expansion at $x/l = 0.03$. The source of the oscillation of the wind-tunnel measurements in the expansion region, $-1.0 < x/l < 0.0$, is unknown, but oscillations in geometry, reference pressure, static pressure, or Mach number are possible. The methods involving ANET propagation have a lower value of pressure in the parabolic expansion region, $-1.0 < x/l < 0.0$, and a lower slope in the shoulder expansion at $x/l = 0.1$, where the parabolic intersects the cylinder. The USM3D–SSGRID results have slight high-frequency waviness in the parabolic expansion region, $-1.0 < x/l < 0.0$. AIRPLANE–ANET predicts nonzero delta pressure in the ambient flow upstream of the nose shock, likely due to dissipation.

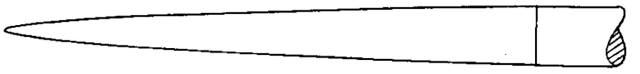

Fig. 16 Parabolic body of revolution geometry [8]. The model is defined as the nose to shoulder, which is 2 in. long.

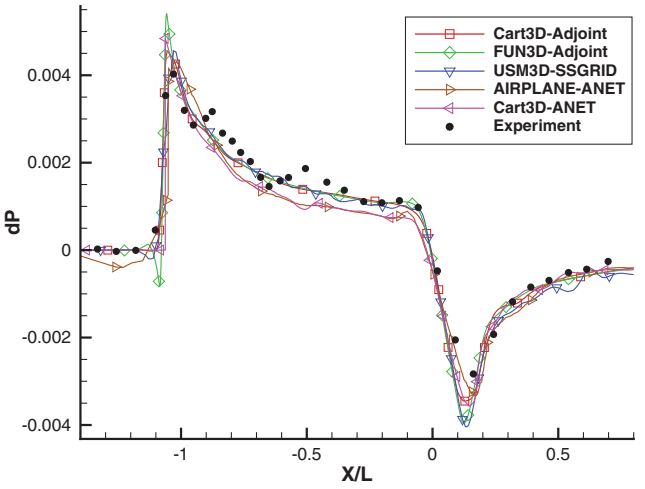

Fig. 17 Nondimensional pressure signature for the parabolic geometry at $h/l = 10.0$.

C. Quartic

The Quartic body of revolution is denoted as Model 5 in Carlson et al. [8]. The radius r of the model as a function of x is

$$r(x) = x^{\frac{1}{4}}\sqrt{\frac{0.04}{\pi\sqrt{2}}} \tag{4}$$

See Fig. 18. The Mach number is 1.41, and the angle of attack is zero. The signature was measured at an altitude of 20 in., which is at 10 body lengths of the 2.0 in. model. This configuration was chosen because it has a strong bow shock and low-boom shape.

The signatures from all methods are compared with experimental measurements digitized from the report [8], which are the filled circles in Fig. 19. The signatures have been shifted slightly in x/l to match pressure at the center of the expansion at $x/l = 0.0$. As with the parabolic shape, the source of the oscillation of the wind-tunnel measurements in the quartic expansion region $-0.75 < x/l < 0.0$ is unknown, but oscillations in geometry, reference pressure, static pressure, or Mach number are possible. All of the methods have very similar bow shock locations and predict the angle of expansion from the maximum overpressure, which implies that they would propagate equivalently to the ground. The methods involving ANET and USM3D–SSGRID have a slight high-frequency oscillation for $-0.75 < x/l < 0.0$.

D. 69 Degree Swept Delta-Wing-Body

The delta-wing–body is denoted as Model 4 in a series of sonic-boom tests of models with different planforms in the report by Hunton et al. [9]. The wing thickness-to-chord ratio is 0.05, and the leading-edge sweep is 69 deg; see Fig. 20. The Mach number is 1.68, and the angle of attack is 4.74 deg to correspond to the data measurement with a lift coefficient of 0.15. The signature was measured at an altitude of 63 cm, which is at 3.6 body lengths of the 17.52 cm model; see Fig. 20. This configuration was chosen because it is a simple lifting geometry.

The sting from the original test [9] is unknown, and it was modeled differently by the participants. Cart3D–adjoint used a 90 deg step to reduce the diameter of the fuselage to the smaller sting. All other participants used a 12 deg cone section to reduce the radius without introducing a backward-facing step or exceeding the maximum turning angle of the flow. The sensitivity of the aft signature to sting

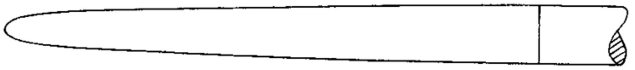

Fig. 18 Quartic body of revolution geometry [8]. The model is defined as the nose to shoulder, which is 2 in. long.

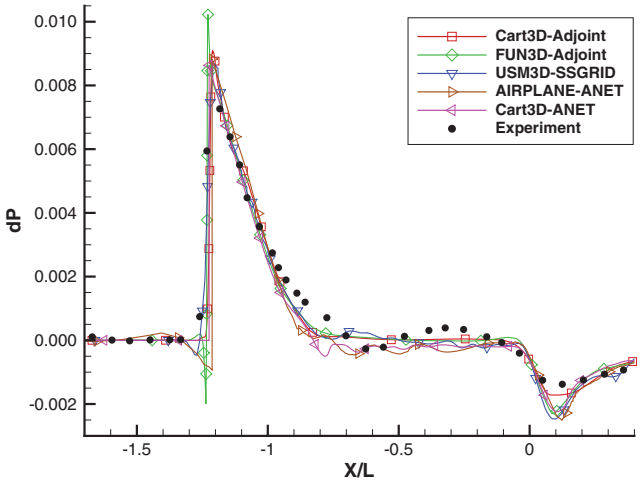

Fig. 19 Nondimensional pressure signature for the quartic geometry at $h/l = 10.0$.

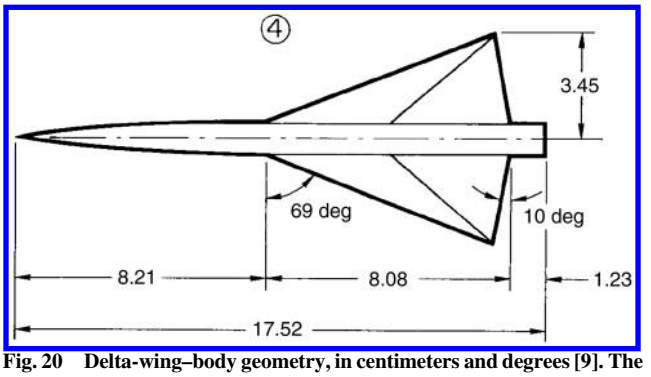

Fig. 20 Delta-wing–body geometry, in centimeters and degrees [9]. The body length is defined as 17.52 cm.

geometry was studied by Cliff and Thomas [13], where the 12 deg cone sting produced a higher-pressure recovery than the 90 deg step.

The wind-tunnel measurements [9] were only available at 3.6 body lengths. Comparisons of the computational methods were also performed at the intermediate locations of 0.2, 0.4, 0.8, 1.2, 2.0, and 2.8 body lengths; see Fig. 21. Data extracted at these intermediate locations facilitated comparisons of the methods and illustrated how the signature attenuates with distance in the near-field region. The direct extractions of the AIRPLANE and Cart3D computed flowfield without the use of ANET are shown for the intermediate locations. The more forward final shock location and higher final pressure recovery for Cart3D–adjoint is likely due to the use of a 90 deg step to reduce the diameter of the fuselage to the smaller sting.

The closest signature to the model was extracted at $h/l = 0.2$, shown in Fig. 22. This signature lacks a simple expansion, and so the signatures have been shifted slightly in x/l to match pressure at the second compression. USM3D–SSGRID shows a slight oscillation in the nose expansion, $0.05 < x/l < 0.4$. The magnitude of this oscillation reduces at further distances. Cart3D–adjoint has the highest sting pressure recovery, $1.0 < x/l$. This higher-pressure recovery moves the last shock forward in Fig. 23 at a $h/l = 0.4$ and further distances. Cart3D–adjoint, FUN3D–adjoint, and USM3D–SSGRID compare favorably with each other and the wind-tunnel measurements ahead of the last shock. AIRPLANE is showing shock thickening at $x/l = 0.4$ and $x/l = 1.0$, which increases at $h/l = 0.8$ (Fig. 24) and $h/l = 1.2$ (Fig. 25). AIRPLANE results are not presented for $h/l = 2.0$ (Fig. 26) and $h/l = 2.8$ (Fig. 27) because the signature has become too diffused.

The signatures from all methods are compared with experimental measurements digitized from the report [9], which are the filled circles in Fig. 28. AIRPLANE–ANET and Cart3D–ANET use the ANET propagation tool for the signatures at 3.6 body lengths. The ANET methods have a higher pressure for $0.9 < x/l < 1.2$ The other three methods have very good agreement until the final shock at $x/l = 1.2$, which may be due to different sting treatments.

This delta-wing–body configuration has been used by a large number of researchers as a validation case. Cheung et al. [12] applied

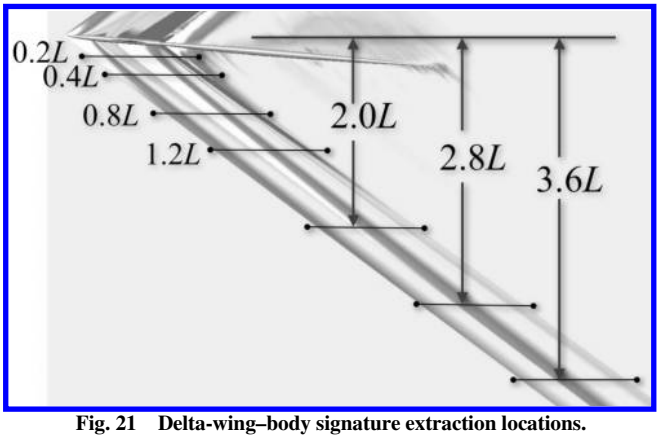

Fig. 21 Delta-wing–body signature extraction locations.

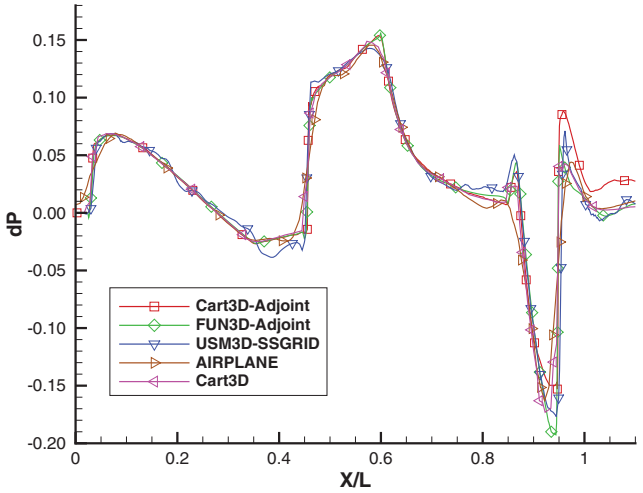

Fig. 22 Nondimensional pressure signature for the delta-wing–body at $h/l = 0.2$.

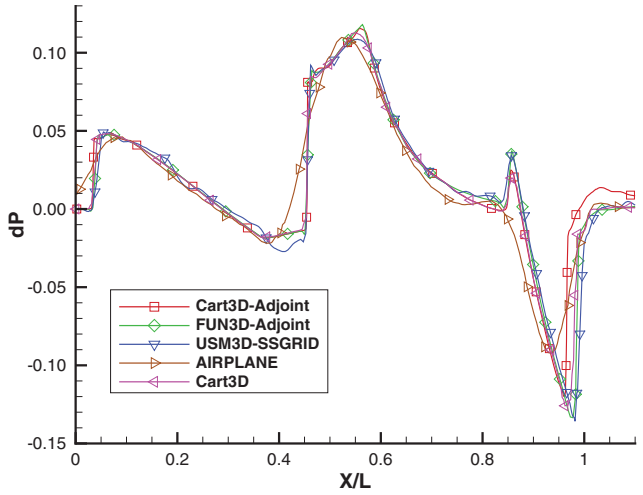

Fig. 23 Nondimensional pressure signature for the delta-wing–body at $h/l = 0.4$.

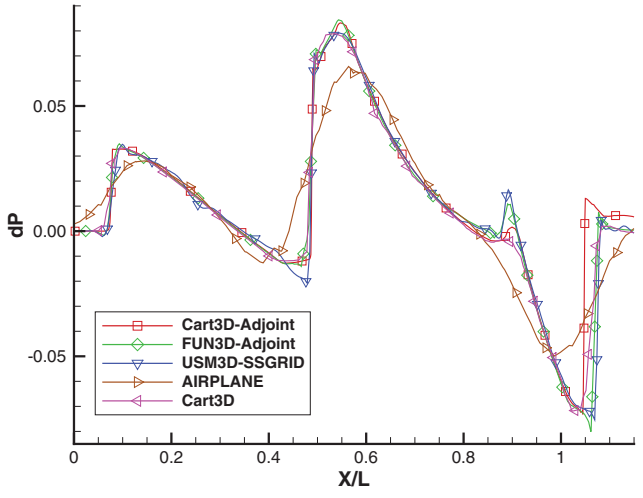

Fig. 24 Nondimensional pressure signature for the delta-wing–body at $h/l = 0.8$.

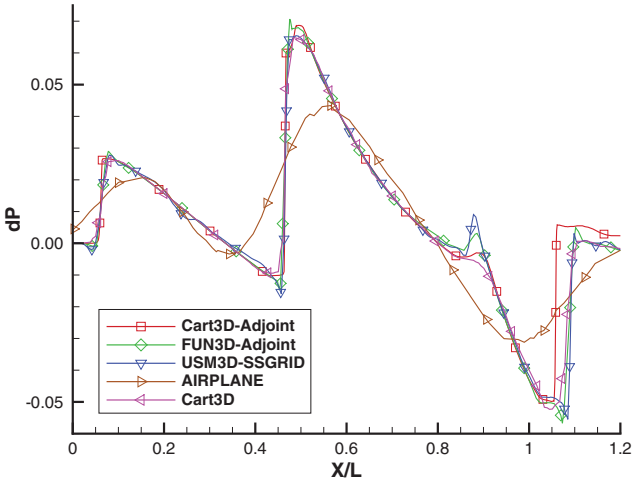

Fig. 25 Nondimensional pressure signature for the delta-wing–body at $h/l = 1.2$.

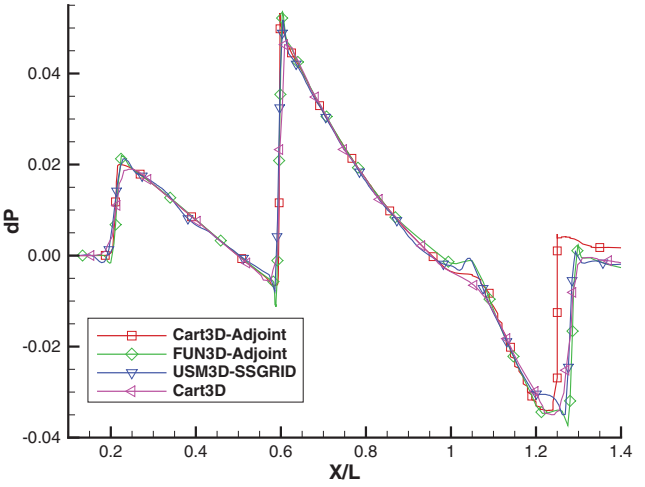

Fig. 26 Nondimensional pressure signature for the delta-wing–body at $h/l = 2.0$.

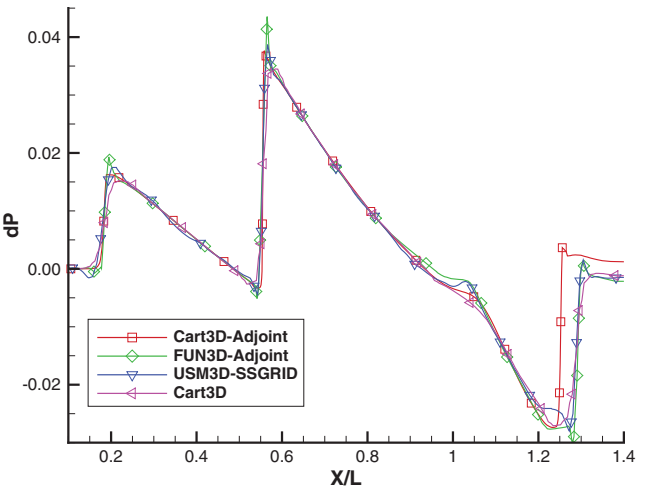

Fig. 27 Nondimensional pressure signature for the delta-wing–body at $h/l = 2.8$.

UPS3D. Cliff and Thomas [13] applied TEAM and AIRPLANE to 0.3 and 0.25 body lengths and propagated these near-field signatures with ANET to the wind-tunnel measurements at 3.6 body lengths. Madson [14] studied various TranAir signature extraction distances and propagated these near-field signatures with ANET to the wind-tunnel measurements at 3.6 body lengths. Djomehri and Erickson [16] applied an adaptive grid FELISA method to 0.3 body lengths, which was propagated with ANET to the wind-tunnel measurement locations. Kandil et al. [58] used PAB3D to 0.4 body lengths and coupled a full potential method to propagate to 3.6 body lengths.

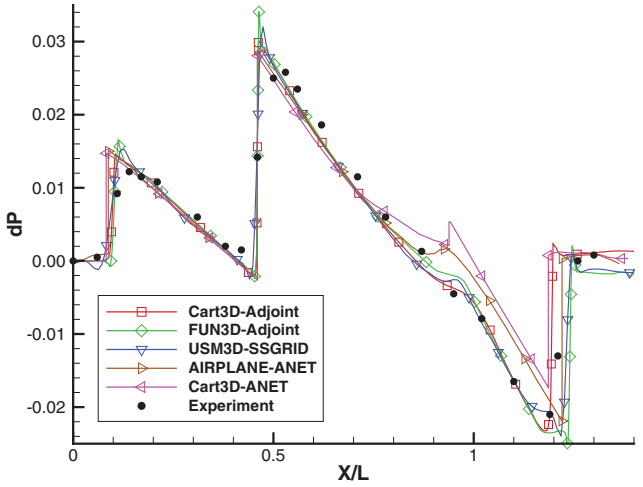

Fig. 28 Nondimensional pressure signature for the delta-wing–body at $h/l = 3.6$.

E. Ames Low Boom Wing Tail with Four Nacelles

The low boom wing tail (LBWT) with nacelles and boundary-layer diverters was chosen as a representative of a complete low sonic-boom configuration; see Fig. 29 for the planform. The LBWT has four nacelles and a length of 12 in. Cliff [15] details the design of the configuration that was later used in a combined simulation and wind-tunnel test campaign by Cliff et al. [10]. Further details of the wind-tunnel test are provided by Mendoza et al. [59]. Siclari and Fouladi [60] also analyzed the LBWT with MIM3DSB.

The signatures from all methods are compared with experimental measurements digitized from Fig. 9a of Cliff et al. [10]. The Mach number is 2.0, and the angle of attack is 2.0 deg. The lift coefficient varied between 0.070 and 0.080 in the wind-tunnel test due to translating the configuration through test section flow angularity. The 2.0 deg angle of attack condition is set to simulate the average lift coefficient of 0.075. The signature was measured at 14 in. below the nose, which is 1.167 body lengths. After the workshop, Durston et al. [55] retested this configuration and measured similar signatures.

The measured signature is compared with the workshop methods in Fig. 30. As with the delta wing, this signature lacks a simple expansion, and so the signatures have been shifted slightly in x/l to match pressure at the second compression attributed to the highly swept inboard wing, $x/l = 0.75$. Details of the signatures aft of $x/l = 1.0$ are provided using an expanded scale in Fig. 31. The various methods agree well with each other and the wind-tunnel measurements forward of $x/l = 1.1$. The location of the shock at $x/l = 1.1$ is similar for all methods, but details aft of that location have a large degree of variation. These aft locations include the influence of the nacelles and boundary-layer diverters. As in the delta-wing case, the various methods used slightly different geometries in the fuselage-sting juncture region. FUN3D–adjoint predicted the most forward location of the shock at $x/l = 1.2$. All of the workshop methods overpredicted the magnitude of this shock. Cart3D–adjoint, FUN3D–adjoint, and USM3D–SSGRID predict a small shock near $x/l = 1.32$ This small shock was not predicted by the ANET methods. The wind-tunnel measurements are too coarse to determine if this shock is present in the wind-tunnel test. The location of the final shock near $x/l = 1.45$ showed the largest variation.

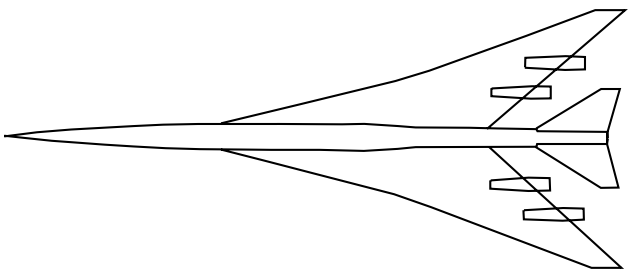

Fig. 29 Planform of the LBWT fuselage, wings, tails, and engines.

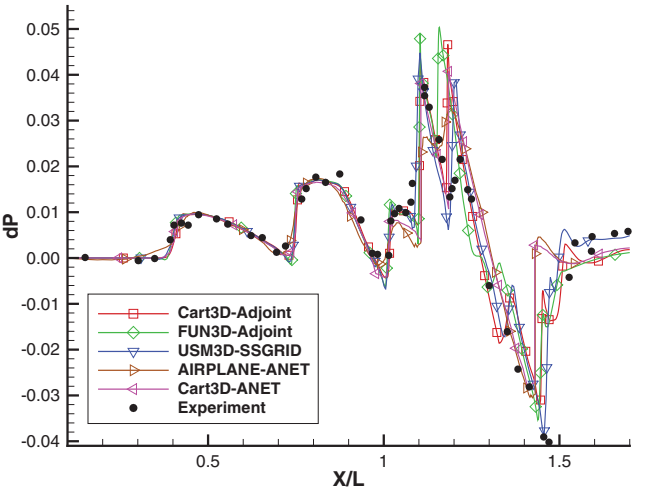

Fig. 30 Entire nondimensional pressure signature for the LBWT at $h/l = 1.167$.

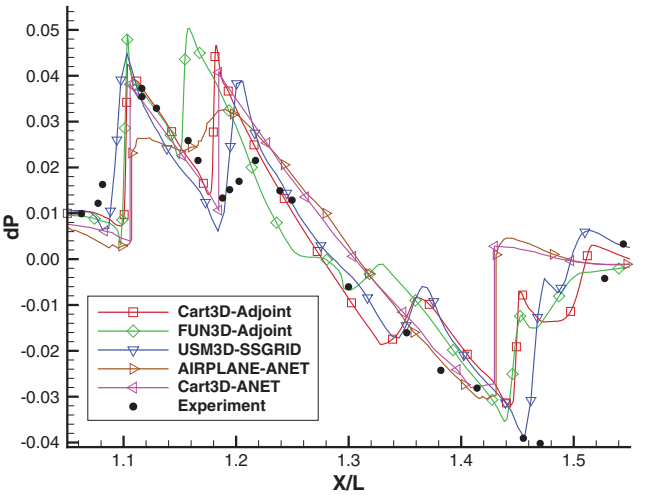

Fig. 31 Center section of the nondimensional pressure signature for the LBWT at $h/l = 1.167$.

V. Execution Time

The execution time required for each of the methods was gathered and reported at the workshop to gauge the resources required. Comparing the required resources is complicated because the analysis was performed on different computer architectures (see Table 3) with a wide range of grid sizes. The adjoint methods used adaptive schemes that included multiple flow and adjoint solves on increasing grid sizes. Estimates of the person hours required to set up and run each of the cases was not recorded. Geometry setup and postprocessing time was also excluded.

Timing data for the cone–cylinder (Table 4) and LBWT (Table 5) configurations are provided. Timing data were also presented at the workshop for the remaining cases but are not provided here in the interest of brevity. These cases are representative of the resources required for the remaining cases. These are execution times as measured in 2008, on computer systems that are significantly slower than currently available systems. The grid generation time in minutes, the solution time in minutes, the solution time in number of CPU minutes, and the final number of control volumes in the grid is provided for each method. Cart3D–adjoint resources are the total of 3–5 flow solutions, adjoint solutions, and grid adaptation steps to reach the final grid. FUN3D–adjoint resources are the total of 8–15 flow solutions, adjoint solutions, and grid adaptation steps to reach

Table 3 Computer architecture descriptions for workshop methods

Method	Grid generation	Solution
Cart3D–adjoint	Eight-core Intel Xeon, 3.2 GHz, 16 GB of memory	Eight-core Intel Xeon, 3.2 GHz, 16 GB of memory
FUN3D–adjoint	One Intel Pentium 4, 3.6 GHz, 2 GB of memory	24 Intel Pentium 4, 3.6 GHz, 2 GB of memory
AIRPLANE–ANET	One processor of an SGI Altix, 1.5 GHz, 1 TB shared memory	64 processors of an SGI Altix, 1.5 GHz, 1 TB shared memory
Cart3D–ANET	One processor of an SGI Altix, 1.5 GHz, 1 TB shared memory	64 processors of an SGI Altix, 1.5 GHz, 1 TB shared memory
USM3D–SSGRID	Single-core Intel Xeon, 3 GHz, 16 GB of memory	48 processors of a SGI Altix, 1.5 GHz, 1 TB shared memory

the final grid. Both the Cart3D–adjoint and FUN3D–adjoint methods have the option of adapting until a specified error level or grid size is reached. The other methods employ a manual grid size request to the grid generation software. Therefore, the exchange of accuracy for cost can be directly controlled by the user for any of these methods. Because of all the factors that affect the resources required for these methods, the information provided should only be used as a guideline and should be treated as extremely case specific and subject to the choices made by the analyst.

Cart3D–adjoint required the least resources of the adaptive methods. Because of the differences in computer hardware, Cart3D–ANET required more CPU-minute resources for a single flow solution than all of the flow and adjoint solutions of Cart3D–adjoint with a final adapted grid of twice the size; see Table 5. The FUN3D–adjoint method required the most resources of the methods presented. An experimental cut-cell algorithm was used in this study, which did not have all of the optimizations that are available to the existing body-fitted grid algorithm. AIRPLANE–ANET was the fastest method but also used the smallest grids. It is possible that a finer grid may improve the AIRPLANE–ANET signatures presented at the workshop at the cost of a longer execution time. USM3D–SSGRID was near the middle of the required resources for some of the largest grids used in the workshop. An evaluation of the effects of reducing USM3D–SSGRID grid size indicated that the required resources can be reduced by as much as a factor of 5 with little loss of accuracy in the boom signatures. The differences in the signatures predicted by the current and reduced-size grids are less than the differences between methods.

VI. Workshop Summary and Recommendations

Five significantly different configurations were selected for the workshop to provide an accurate assessment of each of the workshop methods over a wide range of vehicles (Table 2). These configurations provided signatures with finite rise time, weak shocks, strong stocks, and their combinations. Simple nonlifting to complex lifting configurations were chosen in an attempt to illustrate the differences in the methods. This allowed systematical and incremental increase in complexity toward relevant configurations.

A number of conclusions were drawn at the workshop. The most important is that any of the methods evaluated can produce reasonable results in hours, making them suitable for full configuration analysis and design efforts. It was difficult to form succinct conclusions of the resources required by the methods because different grid sizes and computer architecture were employed. The accuracy of the available methods had improved and exceeded the expectations of the participants. The participants also reported that the automation of the methods was improved as a result of preparing results for the five models. The two adjoint-based adaptation techniques produced identical signatures, except in the extrema, where limiter behavior is important or where the boundary conditions or geometry differed. This indicates that these two independent adaptive methods have reached an engineering level of grid convergence for 3-D Euler flows.

The biggest concern of the workshop results was the scatter in the aft portion of the LBWT. The differences between the codes may indicate that the interactions of the fuselage, wing, tail, and nacelles is harder to predict than those items in isolation. To reduce wind-tunnel measurement uncertainty, a recommendation was made to retest the LBWT to obtain higher-fidelity wind-tunnel data with more resolution of details of the multiple shock signature. Predicting the aft portion of the signatures for complex configuration was known to be a challenge before the workshop [4,18]. Differences in the built and modeled geometry details or an unknown boundary-layer state have been suspected as sources of uncertainty.

VII. Progress After Workshop

Work has continued on improving sonic-boom prediction and using these predictive tools in a design setting. Wayman et al. [57] performed wind-tunnel measurements that included the effect of boundary-layer tripping. Significant changes in the aft portions of the signature were noted, which resulted in a recommendation to consider boundary-layer state in future tests of wind-tunnel models with transitional Reynolds numbers. Viscous effects have been included by multiple researchers. Carter et al. [61] examined a low-boom configuration with laminar and turbulent analysis. Nayani and Campbell [62] showed that the inclusion of viscous effects can drastically improve the prediction of the aft portion of wind-tunnel measurements as compared to inviscid simulation. Elmiligui et al. [63] applied Euler, laminar, and turbulent analysis that included the wind-tunnel walls. Park [64] has extended the 3-D output-based

Table 4 Cone–cylinder execution time and grid size for workshop methods

Method	Grid generation, min	Solution, min	Solution, CPU min	Grid (millions)
Cart3D–adjoint	2.9	38.1	305	3.29
FUN3D–adjoint	1.0	240.0	5760	3.64
AIRPLANE–ANET	4.6	2.1	135	0.31
Cart3D–ANET	2.9	50.7	3246	10.24
USM3D–SSGRID	23.0	40.0	1920	9.70

Table 5 LBWT execution time and grid size for workshop methods

Method	Grid generation, min	Solution, min	Solution, CPU min	Grid (millions)
Cart3D–adjoint	7.2	82.8	662	7.20
FUN3D–adjoint	30.0	720.0	17,280	6.94
AIRPLANE–ANET	12.7	3.7	234	1.06
Cart3D–ANET	3.1	48.4	3,098	3.85
USM3D–SSGRID	50.0	127.0	6,096	15.90

adaptation technique to include viscous effects and examined this configuration. These computational efforts also demonstrated a sensitivity of the signature to analysis using Euler, laminar, and Reynolds-averaged Navier–Stokes with different turbulence models.

Grid generation schemes with a priori freestream shock alignment have been further improved. The MCAP collar grid approach was developed by Cliff et al. [65] and applied to the delta-wing and LBWT configurations. Elmiligui et al. [66] applied MCAP to a wing–body configuration. A new grid generation technique named boom grid also employs a prismatic extrusion approach [62].

To better understand the propulsion effects on sonic boom, Bui [67], Castner [68], and Park and Carlson [69] have included nozzle plumes in simulation. Castner et al. [70] examined the transmission of shocks through nozzle plumes. These propulsion effects have been incorporated into a design environment. Li et al. [52] describes how SSGRID is used for sonic-boom prediction including plume effects in an automated multidisciplinary design environment.

The adjoint-based grid adaptation schemes described at the workshop also enable gradient-based design. Aftosmis et al. [6] used an adjoint-based design method to adjust aircraft outer mold line design to drive near-field signatures to a specified target. Rallabhandi et al. [71,72] have implemented a formal coupling of an adjoint Berger's boom propagation code to an adjoint CFD method. This allows aircraft outer mold line design to drive ground signatures to a specified target or directly reduce A-weighted loudness on the ground.

A continued effort to improve wind-tunnel measurement techniques has accompanied the effort to improve near-field CFD simulation. Multi-orifice pressure rails were developed, which offer increased productivity over single-probe measurements by obtaining the entire signature without the requirement to translate the model in the tunnel. Different individual probes, rails, and data-reduction methods have been documented and tested by Durston et al. [55]. Cliff et al. [73] designed a nonreflective pressure rail (a reflection amplification factor of 1.0) with the aid of CFD. The pressure rail concept enabled an averaging technique, described by Morgenstern [53,54], to correct for spatial flowfield variations, which significantly decreased the signature uncertainty due to tunnel test section flow distortions.

VIII. Conclusions

A summary of the 2008 NASA Sonic Boom Prediction Workshop was provided. The five methods used on the five models were described. These models ranged from simple axisymmetric bodies to full lifting configurations. Using models with a range of complexity illustrated the applicability of the methods and aided identification of areas requiring further development (i.e., the aft signature of complex lifting configurations). The resources required by the methods were reported, but it was difficult to make direct comparisons because different grid sizes and computer architectures were employed by the participants. The workshop was placed in context with a history of methods available to NASA before the workshop and improvements that have been made after the workshop. All workshop methods were found to be sufficient for prediction of near-body signatures and useful for design. The largest difference between the simulated results was in the aft portion of the most complex configuration with wing, fuselage, tail, and nacelles. The simpler configurations with various strength shocks both lifting and nonlifting showed much better agreement between the methods.

References

[1] Bedard, A. J. Jr., "The Measurement of Sonic Boom Waveforms and Propagation Characteristics: Techniques and Challenges," *13th Aeroacoustics Conference*, AIAA Paper 1990-4004, Oct. 1990.

[2] Plotkin, K. J., "State of the Art of Sonic Boom Modeling," *Journal of the Acoustical Society of America*, Vol. 111, No. 1, 2002, pp. 530–536. doi:10.1121/1.1379075

[3] Ozcer, I. A., "Sonic Boom Prediction Using Euler/Full-Potential Methodology," M.S. Thesis, Old Dominion Univ., Norfolk, VA, Dec. 2005.

[4] Park, M. A., "Anisotropic Output-Based Adaptation with Tetrahedral Cut Cells for Compressible Flows," Ph.D. Thesis, Massachusetts Inst. of Technology, Cambridge, MA, Sept. 2008.

[5] Rallabhandi, S. K., "Advanced Sonic Boom Prediction Using the Augmented Burgers Equation," *Journal of Aircraft*, Vol. 48, No. 4, 2011, pp. 1245–1253. doi:10.2514/1.C031248

[6] Aftosmis, M. J., Nemec, M., and Cliff, S. E., "Adjoint-Based Low-Boom Design with Cart3D," *29th AIAA Applied Aerodynamics Conference*, AIAA Paper 2011-3500, June 2011.

[7] Mendoza, J. P., and Hicks, R. M., "Further Studies of the Extrapolation of Near Field Overpressure Data," NASA TM-X-2219, March 1971.

[8] Carlson, H., Mack, R., and Morris, O., "A Wind-Tunnel Investigation of the Effect of Body Shape on Sonic-Boom Pressure Distributions," NASA TN-D-3106, 1965.

[9] Hunton, L. W., Hicks, R. M., and Mendoza, J. P., "Some Effects of Wing Planform on Sonic Boom," NASA TN-D-7160, Jan. 1973.

[10] Cliff, S. E., Baker, T. J., and Hicks, R. M., "Design and Computational/Experimental Analysis of Low Sonic Boom Configurations," *High-Speed Research: 1994 Sonic Boom Workshop: Configuration Design, Analysis, and Testing*, edited by McCurdy, D. A., NASA CP-1999-209699, Dec. 1999, pp. 33–58.

[11] Thomas, C. L., "Extrapolation of Sonic Boom Pressure Signatures by the Waveform Parameter Method," NASA TN-D-6832, June 1972.

[12] Cheung, S. H., Edwards, T. A., and Lawrence, S. L., "Application of Computational Fluid Dynamics to Sonic Boom Near- and Mid-Field Prediction," *Journal of Aircraft*, Vol. 29, No. 5, 1992, pp. 920–926. doi:10.2514/3.46263

[13] Cliff, S. E., and Thomas, S. D., "Euler/Experiment Correlations of Sonic Boom Pressure Signatures," *Journal of Aircraft*, Vol. 30, No. 5, Sept.–Oct. 1993, pp. 669–675. doi:10.2514/3.46396

[14] Madson, M. D., "Sonic Boom Predictions Using a Solution-Adaptive Full-Potential Code," *Journal of Aircraft*, Vol. 31, No. 1, 1994, pp. 57–63. doi:10.2514/3.46455

[15] Cliff, S. E., "On the Design and Analysis of Low Sonic Boom Configurations," *High-Speed Research: Sonic Boom*, Vol. 2, edited by Edwards, T. A., NASA CP-10133, Feb. 1994, pp. 37–78.

[16] Djomehri, M. J., and Erickson, L. L., "An Assessment of the Adaptive Unstructured Tetrahedral Grid, Euler Flow Solver Code FELISA," NASA TP-3526, Dec. 1994.

[17] Fouladi, K., "Unstructured Grids for Sonic-Boom Analysis," *35th Joint Propulsion Conference and Exhibit*, AIAA Paper 1999-2929, June 1999.

[18] Carter, M., and Deere, K., "Grid Sourcing and Adaptation Study Using Unstructured Grids for Supersonic Boom Prediction," *26th AIAA Applied Aerodynamics Conference*, AIAA Paper 2008-6595, Aug. 2008.

[19] Campbell, R., Carter, M., Deere, K., and Waithe, K. A., "Efficient Unstructured Grid Adaptation Methods for Sonic Boom Prediction," *26th AIAA Applied Aerodynamics Conference*, AIAA Paper 2008-7327, Aug. 2008.

[20] Pirzadeh, S. Z., "Advanced Unstructured Grid Generation for Complex Aerodynamic Applications," *26th AIAA Applied Aerodynamics Conference*, AIAA Paper 2008-7178, Aug. 2008.

[21] Park, M. A., "Adjoint-Based, Three-Dimensional Error Prediction and Grid Adaptation," *AIAA Journal*, Vol. 42, No. 9, 2004, pp. 1854–1862. doi:10.2514/1.10051

[22] Lee-Rausch, E. M., Park, M. A., Jones, W. T., Hammond, D. P., and Nielsen, E. J., "Application of a Parallel Adjoint-Based Error Estimation and Anisotropic Grid Adaptation for Three-Dimensional Aerospace Configurations," *23rd AIAA Applied Aerodynamics Conference*, AIAA Paper 2005-4842, June 2005.

[23] Jones, W. T., Nielsen, E. J., and Park, M. A., "Validation of 3D Adjoint Based Error Estimation and Mesh Adaptation for Sonic Boom Prediction," *44th AIAA Aerospace Sciences Meeting and Exhibit*, AIAA Paper 2006-1150, Jan. 2006.

[24] Nemec, M., Aftosmis, M. J., and Wintzer, M., "Adjoint-Based Adaptive Mesh Refinement for Complex Geometries," *46th AIAA Aerospace Sciences Meeting and Exhibit*, AIAA Paper 2008-0725, Jan. 2008.

[25] Aftosmis, M. J., and Berger, M. J., "Multilevel Error Estimation and Adaptive *h*-Refinement for Cartesian Meshes with Embedded Boundaries," *40th AIAA Aerospace Sciences Meeting & Exhibit*, AIAA Paper 2002-0863, Jan. 2002.

[26] Nemec, M., and Aftosmis, M. J., "Adjoint Algorithm for CAD-Based Shape Optimization Using a Cartesian Method," *17th AIAA Computational Fluid Dynamics Conference*, AIAA Paper 2005-4987, June 2005.

[27] Wintzer, M., Nemec, M., and Aftosmis, M. J., "Adjoint-Based Adaptive Mesh Refinement for Sonic Boom Prediction," *26th AIAA Applied Aerodynamics Conference*, AIAA Paper 2008-6593, Aug. 2008.

[28] Thomas, C. L., "Extrapolation of Wind Tunnel Sonic Boom Signatures Without Use of a Waitham F-Function," *Proceedings of the 3rd Conference on Sonic Boom Research*, edited by Schwartz, I. R., NASA SP-225, Jan. 1971, pp. 205–217.

[29] Aftosmis, M. J., Berger, M. J., and Melton, J. E., "Robust and Efficient Cartesian Mesh Generation for Component-Based Geometry," *AIAA Journal*, Vol. 36, No. 6, 1998, pp. 952–960. doi:10.2514/2.464

[30] van Leer, B., "Flux-Vector Splitting for the Euler Equations," *Lecture Notes in Physics*, Vol. 170, 1982, pp. 507–512.

[31] Aftosmis, M. J., Berger, M. J., and Adomavicius, G., "A Parallel Multilevel Method for Adaptively Refined Cartesian Grids with Embedded Boundaries," *38th Aerospace Sciences Meeting and Exhibit*, AIAA Paper 2000-0808, Jan. 2000.

[32] Aftosmis, M. J., Berger, M. J., and Murman, S. M., "Applications of Space-Filling Curves to Cartesian Methods for CFD," *42nd AIAA Aerospace Sciences Meeting and Exhibit*, AIAA Paper 2004-1232, Jan. 2004.

[33] Berger, M. J., Aftosmis, M. J., and Murman, S. M., "Analysis of Slope Limiters on Irregular Grids," *43rd AIAA Aerospace Sciences Meeting and Exhibit*, AIAA Paper 2005-0490, Jan. 2005.

[34] Cliff, S. E., Thomas, S. D., McMullen, M. S., Melton, J. E., and Durston, D. A., "Assessment of Unstructured Euler Methods for Sonic Boom Pressure Signatures Using Grid Refinement and Domain Rotation Methods," NASA TM-2008-214568, Sept. 2008.

[35] Jameson, A., and Baker, T. J., "Improvements to the Aircraft Euler Method," *25th AIAA Aerospace Sciences Meeting*, AIAA Paper 1987-0451, March 1987.

[36] Baker, T. J., "Automatic Mesh Generation for Complex Three-Dimensional Regions Using a Constrained Delaunay Triangulation," *Engineering with Computers*, Vol. 5, Nos. 3–4, 1989, pp. 161–175. doi:10.1007/BF02274210

[37] Nemec, M., and Aftosmis, M. J., "Adjoint Error Estimation and Adaptive Refinement for Embedded-Boundary Cartesian Meshes," *18th AIAA Computational Fluid Dynamics Conference*, AIAA Paper 2007-4187, June 2007.

[38] Venditti, D. A., and Darmofal, D. L., "Grid Adaptation for Functional Outputs: Application to Two-Dimensional Inviscid Flows," *Journal of Computational Physics*, Vol. 176, No. 1, 2002, pp. 40–69. doi:10.1006/jcph.2001.6967

[39] Becker, R., and Rannacher, R., "An Optimal Control Approach to a Posteriori Error Estimation in Finite Element Methods," *Acta Numerica*, Vol. 10, May 2001, pp. 1–102. doi:10.1017/S0962492901000010

[40] Giles, M. B., and Pierce, N. A., "Adjoint Error Correction for Integral Outputs," *Error Estimation and Adaptive Discretization Methods in Computational Fluid Dynamics*, edited by Barth, T. J., and Deconinck, H., Springer, New York, Dec. 2002, pp. 47–96.

[41] Barth, T. J., "A Posteriori Error Estimation and Mesh Adaptivity for Finite Volume and Finite Element Methods," *Adaptive Mesh Refinement — Theory and Applications*, edited by Plewa, T., Linde, T., and Weirs, V. G., Vol. 41, Lecture Notes in Computational Science and Engineering, Springer, New York, 2005, pp. 183–202.

[42] Park, M. A., and Darmofal, D. L., "Validation of an Output-Adaptive, Tetrahedral Cut-Cell Method for Sonic Boom Prediction," *AIAA Journal*, Vol. 48, No. 9, 2010, pp. 1928–1945. doi:10.2514/1.J050111

[43] Park, M. A., and Darmofal, D. L., "Parallel Anisotropic Tetrahedral Adaptation," *46th AIAA Aerospace Sciences Meeting and Exhibit*, AIAA Paper 2008-0917, Jan. 2008.

[44] Venditti, D. A., and Darmofal, D. L., "Anisotropic Grid Adaptation for Functional Outputs: Application to Two-Dimensional Viscous Flows," *Journal of Computational Physics*, Vol. 187, No. 1, 2003, pp. 22–46. doi:10.1016/S0021-9991(03)00074-3

[45] Park, M. A., and Darmofal, D. L., "Output-Adaptive Tetrahedral Cut-Cell Validation for Sonic Boom Prediction," *26th AIAA Applied Aerodynamics Conference*, AIAA Paper 2008-6594, Aug. 2008.

[46] Frink, N. T., Pirzadeh, S. Z., Parikh, P., Pandya, M. J., and Bhat, M. K., "The NASA Tetrahedral Unstructured Software System," *Aeronautical Journal*, Vol. 104, No. 1040, Oct. 2000, pp. 491–499.

[47] Pirzadeh, S. Z., "Three-Dimensional Unstructured Viscous Grids by the Advancing-Layers Method," *AIAA Journal*, Vol. 34, No. 1, 1996, pp. 43–49. doi:10.2514/3.13019

[48] Frink, N. T., "Assessment of an Unstructured-Grid Method for Predicting 3-D Turbulent Viscous Flows," *34th Aerospace Sciences Meeting and Exhibit*, AIAA Paper 1996-0292, Jan. 1996.

[49] Roe, P. L., "Approximate Riemann Solvers, Parameter Vectors, and Difference Schemes," *Journal of Computational Physics*, Vol. 43, No. 2, 1981, pp. 357–372. doi:10.1016/0021-9991(81)90128-5

[50] Samareh, J. A., "GridTool: A Surface Modeling and Grid Generation Tool," *Proceedings of the Workshop on Surface Modeling, Grid Generation, and Related Issues in Computational Fluid Dynamic (CFD) Solutions*, edited by Choo, Y. K., NASA CP-3291, March 1995, pp. 821–831.

[51] Pirzadeh, S. Z., "Structured Background Grids for Generation of Unstructured Grids by Advancing-Front Method," *AIAA Journal*, Vol. 31, No. 2, 1993, pp. 257–265. doi:10.2514/3.11662

[52] Li, W., Campbell, R., Geiselhart, K., Shields, E., Nayani, S., and Shenoy, R., "Integration of Engine, Plume, and CFD Analyses in Conceptual Design of Low-Boom Supersonic Aircraft," *47th AIAA Aerospace Sciences Meeting*, AIAA Paper 2009-1171, Jan. 2009.

[53] Morgenstern, J. M., "How to Accurately Measure Low Sonic Boom or Model Surface Pressures in Supersonic Wind Tunnels," *30th AIAA Applied Aerodynamics Conference*, AIAA Paper 2012-3215, June 2012.

[54] Morgenstern, J. M., "Distortion Correction for Low Sonic Boom Measurement in Wind Tunnels," *30th AIAA Applied Aerodynamics Conference*, AIAA Paper 2012-3216, June 2012.

[55] Durston, D. A., Cliff, S. E., Wayman, T. R., Merret, J. M., Elmiligui, A. A., and Bangert, L. S., "Near-Field Sonic Boom Test on Two Low-Boom Configurations Using Multiple Measurement Techniques at NASA Ames," *29th AIAA Applied Aerodynamics Conference*, AIAA Paper 2011-3333, June 2011.

[56] Carlson, H. W., "Correlation of Sonic-Boom Theory with Wind-Tunnel and Flight Measurements," NASA TR-R-123, Dec. 1964.

[57] Wayman, T. R., Waithe, K. A., Howe, D. C., Bangert, L. S., and Wilcox, F., "Near Field Acoustic Test on a Low Boom Configuration in Langley's 4×4 Wind Tunnel," *29th AIAA Applied Aerodynamics Conference*, AIAA Paper 2011-3331, June 2011.

[58] Kandil, O., Ozcer, I., Zheng, X., and Bobbitt, P., "Comparison of Full-Potential Propagation-Code Computations with the F-5E 'Shaped Sonic Boom Experiment' Program," *43rd AIAA Aerospace Sciences Meeting and Exhibit*, AIAA Paper 2005-0013, Jan. 2005.

[59] Mendoza, J. P., Hicks, R. M., and Cliff, S. E., "Wind Tunnel Sonic Boom Tests on Four High-Speed Civil Transport Models at Mach Numbers from 1.68 to 2.4," NASA TM-2008-214561, Sept. 2008.

[60] Siclari, M. J., and Fouladi, K., "A CFD Study of Component Configuration Effects on the Sonic Boom of Several High-Speed Civil Transport Concepts," *High-Speed Research: Sonic Boom*, Vol. 2, edited by Edwards, T. A., NASA CP-10133, Feb. 1994, pp. 227–299.

[61] Carter, M. B., Campbell, R. L., and Nayani, S. N., "USM3D Analysis of Low Boom Configuration," *29th AIAA Applied Aerodynamics Conference*, AIAA Paper 2011-3335, June 2011.

[62] Nayani, S. N., and Campbell, R. L., "Evaluation of Grid Modification Methods for On- and Off-Track Sonic Boom Analysis," *51st AIAA Aerospace Sciences Meeting*, AIAA Paper 2013-0798, Jan. 2013.

[63] Elmiligui, A., Cliff, S. E., Wilcox, F., Nemec, M., Bangert, L. S., Aftosmis, M. J., and Parlette, E., "Sonic Boom Computations for a Mach 1.6 Cruise Low Boom Configuration and Comparisons with Wind Tunnel Data," *29th AIAA Applied Aerodynamics Conference*, AIAA Paper 2011-3496, June 2011.

[64] Park, M. A., "Low Boom Configuration Analysis with FUN3D Adjoint Simulation Framework," *29th AIAA Applied Aerodynamics Conference*, AIAA Paper 2011-3337, June 2011.

[65] Cliff, S. E., Elmiligui, A. A., Campbell, R. L., and Thomas, S. D., "Evaluation of Refined Tetrahedral Meshes with Projected, Stretched, and Sheared Prism Layers for Sonic Boom Analysis," *29th AIAA Applied Aerodynamics Conference*, AIAA Paper 2011-3338, June 2011.

[66] Elmiligui, A. A., Wilcox, F. J., Cliff, S. E., and Thomas, S. D., "Numerical Predictions of Sonic Boom Signatures for a Straight Line Segmented Leading Edge Model," *7th International Conference on Computational Fluid Dynamics*, Paper ICCFD7-2004, July 2012.

[67] Bui, T. T., "Computational Fluid Dynamics Analysis of Nozzle Plume Effects on Sonic Boom Signature," *Journal of Aircraft*, Vol. 48, No. 2, 2011, pp. 368–380. doi:10.2514/1.C000229

[68] Castner, R. S., "Exhaust Nozzle Plume Effects on Sonic Boom," *Journal of Aircraft*, Vol. 49, No. 2, 2012, pp. 415–422. doi:10.2514/1.C031305

[69] Park, M. A., and Carlson, J.-R., "Turbulent Output-Based Anisotropic Adaptation," *48th AIAA Aerospace Sciences Meeting*, AIAA Paper 2010-0168, Jan. 2010.

[70] Castner, R. S., Elmiligui, A., and Cliff, S., "Exhaust Nozzle Plume and Shock Wave Interaction," *51st AIAA Aerospace Sciences Meeting*, AIAA Paper 2013-0012, Jan. 2013.

[71] Rallabhandi, S. K., "Sonic Boom Adjoint Methodology and Its Applications," *29th AIAA Applied Aerodynamics Conference*, AIAA Paper 2011-3497, June 2011.

[72] Rallabhandi, S. K., Nielsen, E. J., and Diskin, B., "Sonic Boom Mitigation Through Aircraft Design and Adjoint Methodology," *30th AIAA Applied Aerodynamics Conference*, AIAA Paper 2012-3220, June 2012.

[73] Cliff, S. E., Elmiligui, A. A., Aftosmis, M. J., Thomas, S. D., Morgenstern, J. M., and Durston, D. A., "Design and Evaluation of a Pressure Rail for Sonic Boom Measurement in Wind Tunnels," *7th International Conference on Computational Fluid Dynamics*, Paper ICCFD7-2006, July 2012.

This article has been cited by:

1. Joseph W. Connolly, George Kopasakis, Pawel Chwalowski, Jan-Renee Carlson, Mark D. Sanetrik, Walt A. Silva, Jack McNamara. 2020. Aero-Propulso-Elastic Analysis of a Supersonic Transport. *Journal of Aircraft* **57**:4, 569-585. [Abstract] [Full Text] [PDF] [PDF Plus]
2. Rei Yamashita, Lukas Wutschitz, Nikolaos Nikiforakis. 2020. A full-field simulation methodology for sonic boom modeling on adaptive Cartesian cut-cell meshes. *Journal of Computational Physics* **408**, 109271. [Crossref]
3. Thomas K. West IV, Ben D. Phillips. 2020. Multifidelity Uncertainty Quantification of a Commercial Supersonic Transport. *Journal of Aircraft* **57**:3, 491-500. [Abstract] [Full Text] [PDF] [PDF Plus]
4. Marian Nemec, David L. Rodriguez, Michael J. Aftosmis. Adjoint-Based Mesh Adaptation and Shape Optimization for Simulations with Propulsion . [Citation] [PDF] [PDF Plus]
5. Rei Yamashita, Kojiro Suzuki. 2019. Lateral cutoff analysis of sonic boom using full-field simulation. *Aerospace Science and Technology* **88**, 316-328. [Crossref]
6. George R. Anderson, Michael J. Aftosmis, Marian Nemec. 2019. Cart3D Simulations for the Second AIAA Sonic Boom Prediction Workshop. *Journal of Aircraft* **56**:3, 896-911. [Abstract] [Full Text] [PDF] [PDF Plus]
7. Michael A. Park, Marian Nemec. 2019. Nearfield Summary and Statistical Analysis of the Second AIAA Sonic Boom Prediction Workshop. *Journal of Aircraft* **56**:3, 851-875. [Abstract] [Full Text] [PDF] [PDF Plus]
8. Boping Ma, Gang Wang, Zhijin Lei, Zhengyin Ye. 2018. Numerical Investigation of Influence of Mesh Property in Nearfield Sonic Boom Prediction. *Xibei Gongye Daxue Xuebao/Journal of Northwestern Polytechnical University* **36**:5, 865-874. [Crossref]
9. Boping Ma, Gang Wang, Jiong Ren, Zhengyin Ye, Zhijin Lei, Gecheng Zha. 2018. Near-Field Sonic-Boom Prediction and Analysis with Hybrid Grid Navier–Stokes Solver. *Journal of Aircraft* **55**:5, 1890-1904. [Abstract] [Full Text] [PDF] [PDF Plus]
10. Sriram K. Rallabhandi. Sonic Boom Prediction and Mitigation using Three-Dimensional Earth Effects . [Citation] [PDF] [PDF Plus]
11. Thomas K. West, Ben D. Phillips. Multifidelity Uncertainty Quantification of a Commercial Supersonic Transport . [Citation] [PDF] [PDF Plus]
12. Rei Yamashita, Kojiro Suzuki. 2018. Rise Time Prediction of Sonic Boom by Full-Field Simulation. *Journal of Aircraft* **55**:3, 1305-1310. [Citation] [Full Text] [PDF] [PDF Plus]
13. Takashi Misaka, Shigeru Obayashi. 2017. Numerical study on jet-wake vortex interaction of aircraft configuration. *Aerospace Science and Technology* **70**, 615-625. [Crossref]
14. Michael A. Park, Marian Nemec. Near Field Summary and Statistical Analysis of the Second AIAA Sonic Boom Prediction Workshop . [Citation] [PDF] [PDF Plus]
15. George Anderson, Michael J. Aftosmis, Marian Nemec. Cart3D Simulations for the Second AIAA Sonic Boom Prediction Workshop . [Citation] [PDF] [PDF Plus]
16. Sriram K. Rallabhandi, Michael A. Park. Adjoint-Based Mesh Adaptation for the Sonic Boom Signature Loudness . [Citation] [PDF] [PDF Plus]
17. Boping Ma, Gang Wang, Jiong Ren, Zhengyin Ye, Gecheng Zha. Near Field Sonic Boom Analysis with HUNS3D Solver . [Citation] [PDF] [PDF Plus]
18. Thomas K. West IV, Bryan W. Reuter, Eric L. Walker, Bil Kleb, Michael A. Park. 2017. Uncertainty Quantification and Certification Prediction of Low-Boom Supersonic Aircraft Configurations. *Journal of Aircraft* **54**:1, 40-53. [Abstract] [Full Text] [PDF] [PDF Plus]
19. Rei Yamashita, Kojiro Suzuki. 2016. Full-Field Sonic Boom Simulation in Stratified Atmosphere. *AIAA Journal* **54**:10, 3223-3231. [Abstract] [Full Text] [PDF] [PDF Plus]
20. Michael A. Park, John M. Morgenstern. 2016. Summary and Statistical Analysis of the First AIAA Sonic Boom Prediction Workshop. *Journal of Aircraft* **53**:2, 578-598. [Abstract] [Full Text] [PDF] [PDF Plus]
21. Jason Pearl, Melissa B. Carter, Alaa A. Elmiligui, Courtney S. Winski, Sudheer Nayani. Numerical Examination of Shock Generator Geometries and Nozzle Plume Effects on Pressure Signature . [Citation] [PDF] [PDF Plus]
22. Michael A. Park, Adrien Loseille, Joshua A. Krakos, Todd R. Michal. Comparing Anisotropic Output-Based Grid Adaptation Methods by Decomposition
 . [Citation] [PDF] [PDF Plus]

23. Balaji Shankar Venkatachari, Michael Mullane, Gary Cheng, Chau-Lyan Chang. Numerical Study of Counterflowing Jet Effects on Supersonic Slender-Body Configurations . [Citation] [PDF] [PDF Plus]